

ARMY RESEARCH LABORATORY



## **A Model for Deformation and Fragmentation in Crushable Brittle Solids**

**by John D. Clayton**

**ARL-RP-201**

**March 2008**

**A reprint from the *International Journal of Impact Engineering*,  
vol. 35, pp. 269–289, 2008.**

## **NOTICES**

### **Disclaimers**

The findings in this report are not to be construed as an official Department of the Army position unless so designated by other authorized documents.

Citation of manufacturer's or trade names does not constitute an official endorsement or approval of the use thereof.

Destroy this report when it is no longer needed. Do not return it to the originator.

# **Army Research Laboratory**

Aberdeen Proving Ground, MD 21005-5069

---

---

**ARL-RP-201**

**March 2008**

---

---

## **A Model for Deformation and Fragmentation in Crushable Brittle Solids**

**John D. Clayton**  
**Weapons and Materials Research Directorate, ARL**

A reprint from the *International Journal of Impact Engineering*,  
vol. 35, pp. 269–289, 2008.

REPORT DOCUMENTATION PAGE			Form Approved OMB No. 0704-0188		
Public reporting burden for this collection of information is estimated to average 1 hour per response, including the time for reviewing instructions, searching existing data sources, gathering and maintaining the data needed, and completing and reviewing the collection information. Send comments regarding this burden estimate or any other aspect of this collection of information, including suggestions for reducing the burden, to Department of Defense, Washington Headquarters Services, Directorate for Information Operations and Reports (0704-0188), 1215 Jefferson Davis Highway, Suite 1204, Arlington, VA 22202-4302. Respondents should be aware that notwithstanding any other provision of law, no person shall be subject to any penalty for failing to comply with a collection of information if it does not display a currently valid OMB control number. <b>PLEASE DO NOT RETURN YOUR FORM TO THE ABOVE ADDRESS.</b>					
1. REPORT DATE (DD-MM-YYYY) March 2008		2. REPORT TYPE Reprint		3. DATES COVERED (From - To) October 2006–October 2007	
4. TITLE AND SUBTITLE A Model for Deformation and Fragmentation in Crushable Brittle Solids			5a. CONTRACT NUMBER		
			5b. GRANT NUMBER		
			5c. PROGRAM ELEMENT NUMBER		
6. AUTHOR(S) John D. Clayton			5d. PROJECT NUMBER WHPR01E		
			5e. TASK NUMBER		
			5f. WORK UNIT NUMBER		
7. PERFORMING ORGANIZATION NAME(S) AND ADDRESS(ES) U.S. Army Research Laboratory ATTN: AMSRD-ARL-WM-TD Aberdeen Proving Ground, MD 21005-5069			8. PERFORMING ORGANIZATION REPORT NUMBER ARL-RP-201		
9. SPONSORING/MONITORING AGENCY NAME(S) AND ADDRESS(ES)			10. SPONSOR/MONITOR'S ACRONYM(S)		
			11. SPONSOR/MONITOR'S REPORT NUMBER(S)		
12. DISTRIBUTION/AVAILABILITY STATEMENT Approved for public release; distribution is unlimited.					
13. SUPPLEMENTARY NOTES A reprint from the <i>International Journal of Impact Engineering</i> , vol. 35, pp. 269–289, 2008.					
14. ABSTRACT A unified framework of continuum elasticity, inelasticity, damage mechanics, and fragmentation in crushable solid materials is presented. A free energy function accounts for thermodynamics of elastic deformation and damage, and thermodynamically admissible kinetic relations are given for inelastic rates (i.e., irreversible strain and damage evolution). The model is further specialized to study concrete subjected to ballistic loading. Numerical implementation proceeds within a finite element context in which standard continuum elements represent the intact solid and particle methods capture eroded material. The impact of a metallic, spherical projectile upon a planar concrete target and the subsequent motion of the resulting cloud of concrete debris are simulated. Favorable quantitative comparisons are made between the results of simulations and experiments regarding residual velocity of the penetrator, mass of destroyed material, and crater and hole sizes in the target. The model qualitatively predicts aspects of the fragment cloud observed in high-speed photographs of the impact experiment, including features of the size and velocity distributions of the fragments. Additionally, two distinct methods are evaluated for quantitatively characterizing the mass and velocity distributions of the debris field, with one method based upon a local energy balance and the second based upon global entropy maximization. Finally, the model is used to predict distributions of fragment masses produced during impact crushing of a concrete sphere, with modest quantitative agreement observed between results of simulation and experiment.					
15. SUBJECT TERMS fragmentation, damage mechanics, thermodynamics, statistical physics, concrete					
16. SECURITY CLASSIFICATION OF:			17. LIMITATION OF ABSTRACT	18. NUMBER OF PAGES	19a. NAME OF RESPONSIBLE PERSON John D. Clayton
a. REPORT UNCLASSIFIED	b. ABSTRACT UNCLASSIFIED	c. THIS PAGE UNCLASSIFIED	UL	28	19b. TELEPHONE NUMBER (Include area code) 410-306-0975

# A model for deformation and fragmentation in crushable brittle solids

John D. Clayton\*

*US Army Research Laboratory, Impact Physics Branch, AMSRD-ARL-WM-TD, Aberdeen Proving Ground, MD 21005-5069, USA*

Received 14 November 2006; received in revised form 9 February 2007; accepted 18 February 2007

Available online 12 March 2007

## Abstract

A unified framework of continuum elasticity, inelasticity, damage mechanics, and fragmentation in crushable solid materials is presented. A free energy function accounts for thermodynamics of elastic deformation and damage, and thermodynamically admissible kinetic relations are given for inelastic rates (i.e., irreversible strain and damage evolution). The model is further specialized to study concrete subjected to ballistic loading. Numerical implementation proceeds within a finite element context in which standard continuum elements represent the intact solid and particle methods capture eroded material. The impact of a metallic, spherical projectile upon a planar concrete target and the subsequent motion of the resulting cloud of concrete debris are simulated. Favorable quantitative comparisons are made between the results of simulations and experiments regarding residual velocity of the penetrator, mass of destroyed material, and crater and hole sizes in the target. The model qualitatively predicts aspects of the fragment cloud observed in high-speed photographs of the impact experiment, including features of the size and velocity distributions of the fragments. Additionally, two distinct methods are evaluated for quantitatively characterizing the mass and velocity distributions of the debris field, with one method based upon a local energy balance and the second based upon global entropy maximization. Finally, the model is used to predict distributions of fragment masses produced during impact crushing of a concrete sphere, with modest quantitative agreement observed between results of simulation and experiment.

© 2007 Elsevier Ltd. All rights reserved.

*Keywords:* Fragmentation; Damage mechanics; Thermodynamics; Statistical physics; Concrete

## 1. Introduction

An understanding of dynamic deformation, damage evolution, and fragmentation of solid materials is needed in order to describe complex physical phenomena occurring, for example, in solid body collisions and ballistic impacts. In the context of wartime environments or terrorist attacks, injuries to soldiers and bystanders due to flying concrete debris as a result of violently explosive destruction of buildings and other urban structures have been reported [1]. Characterization of the debris field would enable enhancement of current protective strategies, for example improvements in body armor and guidelines on safe stand-off distances from buildings undergoing detonation or pulverization [2]. The defense industry also has a need to more fully understand the material failure process so that

strategies may be improved to defeat fortified concrete structures such as reinforced walls, bunkers, and road-blocks. Finally, crushing processes for rubble obtained from demolished urban structures (for recycling purposes) drive the development of mathematical models enabling an increased understanding of inelastic deformation, fracture, and fragmentation of concrete-based materials [3–5].

The aim of the present study is development of a self-consistent theory accounting for dynamic deformation, damage, and fragmentation mechanisms, specifically amenable to brittle, crushable solids such as concrete, mortar, and cinder block. This theory enables simulation and analysis of urban structures undergoing ballistic or explosive loading scenarios. These materials are referred to here as ‘crushable’ since they nominally contain significant initial porosity. For example, the microstructure of concrete consists of a mixture of aggregate stones, typically granite, quartz, or limestone, embedded in a cement matrix. The matrix, alternatively referred to as

\*Tel.: +1 410 306 0975; fax: +1 410 306 0783.

E-mail address: [jclayton@arl.army.mil](mailto:jclayton@arl.army.mil).

‘mortar’, consists of sand, water, ash, and various binding agents. Porosities on the order of 10–20% in standardized concretes used for urban construction are not uncommon [6–8], and the pores may be air- or water-filled depending on the preparation method and moisture of the ambient environment. This initial porosity induces a pressure dependency in the effective compressive bulk modulus, with the stiffness of the material increasing as the pores are compacted.

A voluminous literature exists describing mechanical properties and constitutive modeling of concrete. A brief survey of recent work deemed most relevant to the present research is given here. Hanchak et al. [6] conducted laboratory triaxial tests and coupled pressure-shear experiments, in addition to ballistic perforation measurements. Holmquist et al. [7] developed a constitutive model (HJC model), with the pressure–volume response following data from [6], and a plasticity and damage model reminiscent, yet not identical, to those used previously for metallic materials [9], with failure criteria based on cumulative strain measures [10]. Grote et al. [11] used uniaxial stress tests, split Hopkinson bar tests, and plate impact tests to measure the rate-dependent compressive flow strength of concrete and mortar at low, intermediate, and high strain rates, respectively. Properties were subsequently used in dynamic finite element simulations of plate impact of the dual-phase concrete [12], in which microstructures were resolved explicitly, with an extended Drucker–Prager plasticity theory used to capture pressure-dependent yield. Bažant et al. [13] developed a model for concrete in which plastic slip may occur on a number of microplanes, somewhat analogous to the slip planes of crystal plasticity theory [14]. This model has been applied to address a number of features of concrete behavior arising in impact events, including high deformation rates [15] and finite strains [16]. Other bounding surface-based models addressing yielding or damage under a variety of static and cyclic stress state histories have been formulated [17,18]. The variability in mechanical properties such as flow stress and fracture toughness with microstructure constituents [19], processing conditions (e.g., environment and geographic location), and age of the material presents an inherent difficulty in precisely modeling the mechanical behavior of this class of urban structural materials.

The theoretical framework for the behavior of crushable solids formulated here differs from many existing concrete constitutive models in its usage of a multiplicative split of the deformation gradient into elastic and inelastic components [20] and its emphasized adherence to the laws of continuum mechanics and thermodynamics, including the entropy production inequality (i.e., second law of thermodynamics). This is not meant to imply that existing engineering models developed elsewhere for concrete material behavior do not satisfy thermodynamic principles, merely that such principles are often not considered explicitly in the process of model development and parameter selection. In the present work, thermodynami-

cally consistent properties and evolution equations for porosity and damage are formulated following the general procedures of [21,22]. This approach, with multiplicative finite deformation kinematics and simultaneous adherence to energy conservation and entropy production, has been used frequently for metal plasticity [23,24]. However, its use in urban structural materials such as concrete has not heretofore been emphasized in the literature, though some analogous thermodynamic aspects have been incorporated for modeling geological materials [25]. The present model also invokes the concept of an internal state variable representing damage in the material, related to the normalized density of micro-cracks in the substance. Similar approaches, albeit with various different ways of relating continuum damage variables to microscopic damage entities or flaws, have been used for some time in continuum damage mechanics theories [26–30]. Mathematically consistent constitutive models for elastic and inelastic deformation mechanisms, including phase changes, in moderately porous solids have also been developed elsewhere [31,32].

In the numerical implementation of the model developed here, elastic strains are assumed to remain small in order to permit computational efficiency in an explicit integration scheme, as is common in hydrocodes used to simulate finite plastic deformation of metals [33]. While some consistency with the theoretical formulation is lost in this approach, as opposed to a more costly, yet more rigorous implicit formulation for finite elasticity [34], possible limitations in accuracy due to elastic nonlinearity are thought to be more apparent here than would be the case if small elastic deformations were assumed from the outset in both theory and implementation.

A variety of numerical approaches have been undertaken to numerically simulate ballistic impact and fragmentation. Conventional finite element methods have been used for decades to model penetration, including concrete targets [7,16]. Often, elements are deleted or eroded when some failure criteria or maximum cumulative strain is achieved. Fragmentation has been addressed in this context via post-processing calculations [35,36]. More recently, cohesive finite elements have been used to simulate dynamic fragmentation [37,38]. This technique is naturally more realistic than element deletion for modeling discrete cracks, and is thought to be particularly useful for simulations of microstructure-level fracture along grain boundaries and other internal interfaces, for example, where cohesive elements can be inserted along weak links in the microstructure [24,39]. The discrete element method, whereby material elements are connected by spring-like entities, has been used to simulate dynamic deformation and fracture of concrete [40]. Eulerian representations of material behavior have also been implemented to characterize fragment debris subsequent to ballistic impact [41,42]. Such approaches offer advantages with regards to addressing fluid-like flow of material at high pressures. Particle methods have also been used to address fracture and fragmentation.

Silling and Askari [43] implemented a theory in which the governing equations are cast in integral form. Smooth particle hydrodynamics (SPH) methods [44,45] permit simulations of very large distortions in ballistic impact in a Lagrangian setting, with local continuum-type quantities such as deformation rates depending upon relative particle motions and smoothing functions. Concrete subjected to explosive loading has been modeled with SPH [45]. The approach followed here is that of Johnson et al. [46,47], in which continuum finite elements are converted to meshless particles when specified erosion criteria are met. To this end, the generalized particle algorithm (GPA) of the EPIC 2003 code is used; GPA differs from SPH regarding the choice of smoothing functions [46]. This method is computationally efficient and appears natural for modeling fragmentation, as the particle velocities and trajectories can be directly associated with those of the fragments of comminuted material. However, information regarding sizes of individual fragments is not readily available from standard SPH or GPA methods, since the mass of each particle is simply the nodal mass, which in turn depends upon the discretization. For example, a uniform grid would produce a uniform size/mass distribution of particles. This issue is addressed here by incorporating additional physics into the constitutive framework permitting calculation of non-uniform fragment mass distributions.

A number of analytical methods have been developed to quantitatively characterize fragmentation. Grady [48] suggested that the total energy of a fragmenting body consists of expansion kinetic energy and the surface or fracture energy, the latter an intrinsic material property. Energy minimization under variations of fragment dimension then yield the nominal fragment size for spherical expansion of a fluid or brittle tensile fracture of a solid. A more extensive treatment was later given in [49]. Grady's approach was extended by Glenn and Chudnovsky [50] to include stored elastic energy and then Johnson and Cook [35] to account for 3D stress states, though in these latter approaches a direct energy balance was used, as opposed to energy minimization. In a finite element implementation, Johnson and Cook [35] computed a cumulative fragment size based on the strain and strain-rate history in the material, though the fragmentation process was perhaps unrealistically assumed to commence in each element from the outset of local deformation, and the fragmentation energy consumed did not enter the constitutive model for the bulk material behavior. Miller et al. [51] demonstrated the history dependence of fragment size using a numerical approach with cohesive fracture and developed an analytical model of fragmentation for a body with a time-dependent stress history. Analytical models have also been developed to characterize statistical distributions of fragment sizes. These include methods based on random disintegration of bodies in one or more dimensions leading to Poisson-type statistics, as well as geometry-based approaches partitioning areas or volumes in various ways [52,53]. Entropy maximization principles, by which the

most chaotic distributions are deemed most probable, have also been used to construct fragment statistics [53] including methods accounting for elastic energy and damage [54] and rotational inertia thought important for granular microstructures [55]. Continuum micromechanics-based models in which crack sizes are related to typical fragment sizes in dynamically fracturing brittle materials have also been developed [56].

Previous efforts toward modeling ballistic fragmentation with Lagrangian or Eulerian hydrocodes have often focused on metallic targets [35,41,42]. Implementations for modeling fragmentation characteristics of concrete or geological materials have also been reported [2,36]. In the present work, two alternative methods are considered for computing fragment size and velocity statistics, both compatible with the laws of thermodynamics and momentum conservation. The first relies on a local energy balance similar to that of [35,48–50], but newly applied to crushable solids in a method consistent with the description of energy in the bulk constitutive model. Fracture energy is explicitly accounted for in the constitutive model, via evolution of an internal variable representing damage in the substance, and fuels the fragmentation process when damage reaches a critical level. In this way, energy consumed in fragmentation is not a static intrinsic property, but depends on the damage progression in the material. The distribution of mass of the fragments is then computed by application of the energy balance to converted particles in the simulation, with the velocity distribution of the fragments associated with that of the particles. In the second approach, a method based on entropy maximization and classical statistical physics is applied, following [53,57]. A joint probability distribution function for fragment mass and velocity is derived consistent with energy and momentum conservation, with the global kinetic energy and trajectory of the fragment cloud computed from the mass-weighted average velocity of the ensemble of converted particles.

The remainder of this paper is organized as follows. The continuum theory is presented, consisting of kinematics, thermodynamics, and kinetic relations. Then fragmentation modeling is discussed, including methods based on a local energy balance or global statistical physics. Features that differentiate the present theory from others in the literature are embedded in these descriptions. Model parameters for a particular mix of concrete are given, and the implementation in a finite element setting with particle dynamics is then described. The model is first used to simulate high-speed perforation of a concrete target by a tungsten sphere. Numerical results are interpreted and compared with experimental quantities and observations from high-speed photography [58]. A second simulation is also performed, whereby a concrete sphere is impacted against a fixed plate at a moderate velocity; resultant fragment masses are computed using the local energetic theory and compared with experimental data from [3].

The following notation is invoked. Cartesian coordinates are applied throughout, with summation implied over

repeated indices. Vector and tensor quantities are represented with boldface type, while scalars and individual components of tensors are written in italics. Juxtaposition implies summation over two repeated adjacent indices (e.g.,  $(\mathbf{AB})_{ab} = A_{ac}B_{cb}$ ). The scalar product of vectors is represented by the symbol ‘ $\cdot$ ’ (e.g.,  $\mathbf{a} \cdot \mathbf{b} = a_a b_a$ ). The colon denotes contraction over repeated pairs of indices (e.g.,  $\mathbf{A} : \mathbf{B} = \text{tr}(\mathbf{A}^T \mathbf{B}) = A_{ab} B_{ab}$ , where ‘tr’ is the trace operation, and  $\mathbf{C} : \mathbf{A} = C_{abcd} A_{cd}$ ). Superposed  $-1$ , T, and ‘ $\cdot$ ’ denote inverse, transpose, and material time derivative, respectively. Additional notation is defined as it appears in the text.

## 2. Continuum modeling

Aspects of the model framework for describing deforming and fragmenting crushable solids are presented here. The kinematic framework is general in the sense that it is intended for applications involving any solid material exhibiting similar deformation mechanisms.

The kinematic description begins with a multiplicative decomposition of the deformation gradient  $\mathbf{F}$ :

$$\mathbf{F} = \partial \mathbf{x} / \partial \mathbf{X} = \mathbf{F}^E \mathbf{F}^D, \quad (1)$$

where  $\mathbf{x}$  and  $\mathbf{X}$  denote spatial and reference coordinates in 3D Euclidean space,  $\mathbf{F}^E$  is the recoverable elastic deformation, and  $\mathbf{F}^D$  is the irreversible deformation associated with defects such as micro-cracks, voids, dislocations, or shear discontinuities evolving within the material. The spatial velocity gradient then follows directly from (1) as

$$\mathbf{L} = \partial \dot{\mathbf{x}} / \partial \mathbf{x} = \underbrace{\dot{\mathbf{F}}^E \mathbf{F}^{E-1}}_{\mathbf{L}^E} + \underbrace{\mathbf{F}^E \dot{\mathbf{F}}^D \mathbf{F}^{D-1} \mathbf{F}^{E-1}}_{\mathbf{L}^D}. \quad (2)$$

The irreversible volumetric deformation associated with pore collapse in crushable materials is described by

$$\varphi = J^{D-1} - 1, \quad J^D = \det \mathbf{F}^D, \quad (3)$$

where  $\varphi$  is the volume reduction upon crushing, a positive quantity when the volume is reduced. Inelastic volumetric expansion would be captured by  $\varphi < 0$ ; however, such an effect is not considered explicitly in the specific material model that follows, since any inelastic tensile volumetric deformations are assumed here to remain infinitesimal and negligible for brittle solids undergoing dynamic fracture. The inelastic velocity gradient from (2) can be written as

$$\mathbf{L}^D = \mathbf{F}^E \dot{\mathbf{F}}^D \mathbf{F}^{D-1} \mathbf{F}^{E-1} = \hat{\mathbf{L}}^D - \frac{1}{3} \dot{\varphi} (1 + \varphi)^{-1} \mathbf{1}, \quad (4)$$

where  $\hat{\mathbf{L}}^D$  is the deviatoric inelastic velocity gradient mapped to the spatial frame and  $\mathbf{1}$  is the identity map. The elastic strain tensor and scalar measure of volumetric elastic strain in the intermediate configuration are defined as

$$2\mathbf{E}^E = \mathbf{F}^{ET} \mathbf{F}^E - \mathbf{1}, \quad \vartheta_E = \text{tr} \mathbf{E}^E. \quad (5)$$

Standard local balances of mass, linear and angular momentum apply:

$$\rho_0 = \rho J = \rho \det \mathbf{F}, \quad \text{div} \boldsymbol{\sigma} + \mathbf{f} = \rho \ddot{\mathbf{x}}, \quad \boldsymbol{\sigma} = \boldsymbol{\sigma}^T, \quad (6)$$

where  $\mathbf{f}$  is the body force vector per unit spatial volume,  $\boldsymbol{\sigma}$  is the Cauchy stress, and  $\text{div}$  denotes divergence in the spatial frame. The spatial energy balance is written in localized form as

$$\rho \dot{e} = \boldsymbol{\sigma} : \mathbf{L} - \text{div} \mathbf{q} \quad (7)$$

with  $e$  the internal energy per unit mass and  $\mathbf{q}$  the heat flux vector. The second law of thermodynamics is stated as

$$\boldsymbol{\sigma} : \mathbf{L} - \theta^{-1} \mathbf{q} \cdot \partial_{\mathbf{x}} \theta \geq \rho (\dot{\psi} + \dot{\theta} \eta), \quad (8)$$

where  $\theta$  is the temperature,  $\eta$  is the entropy per unit mass, and the Helmholtz free energy is  $\psi = e - \theta \eta$ . The spatial gradient operator is written as  $\partial_{\mathbf{x}}$ .

The Helmholtz free energy, on a per unit mass basis, is assumed to exhibit the following general functional dependency:

$$\psi = \psi(\mathbf{E}^E, \varphi, \theta, D), \quad (9)$$

where  $D$  is a scalar internal state variable representing cumulative damage in the material typically occurring in conjunction with inelastic deformation. Stress-strain and temperature-entropy relations are then deduced as [21,22]

$$\boldsymbol{\sigma} = \mathbf{F}^E \rho \frac{\partial \psi}{\partial \mathbf{E}^E} \mathbf{F}^{ET}, \quad \eta = -\frac{\partial \psi}{\partial \theta}. \quad (10)$$

The dissipation inequality (8) becomes

$$\boldsymbol{\sigma} : \hat{\mathbf{L}}^D + \left( \frac{p}{1 + \varphi} - \rho \frac{\partial \psi}{\partial \varphi} \right) \dot{\varphi} - \rho \frac{\partial \psi}{\partial D} \dot{D} \geq \theta^{-1} \mathbf{q} \cdot \partial_{\mathbf{x}} \theta, \quad (11)$$

where the Cauchy pressure  $3p = -\text{tr} \boldsymbol{\sigma}$ . Assuming isotropic heat conduction in the spatial frame,

$$\mathbf{q} = -\kappa \partial_{\mathbf{x}} \theta, \quad (12)$$

with  $\kappa$  the scalar thermal conductivity, and defining the specific heat parameter  $\hat{c} = \partial e / \partial \theta = -\theta \partial^2 \psi / \partial \theta^2$ , the energy balance can be written in terms of temperature rise  $\hat{\theta}$  as

$$\rho \hat{c} \hat{\theta} = \boldsymbol{\sigma} : \mathbf{L}^D - \rho \left[ \left( \frac{\partial \psi}{\partial \varphi} - \theta \frac{\partial^2 \psi}{\partial \theta \partial \varphi} \right) \dot{\varphi} - \left( \frac{\partial \psi}{\partial D} - \theta \frac{\partial^2 \psi}{\partial \theta \partial D} \right) \dot{D} - \theta \frac{\partial \psi}{\partial \theta \partial \mathbf{E}^E} : \dot{\mathbf{E}}^E \right] + \text{div}(\kappa \partial_{\mathbf{x}} \theta). \quad (13)$$

The framework is now specialized to brittle crushable solids such as concrete and mortar, with deformations comprising  $\mathbf{F}^D$  associated with micro-crack opening and sliding, as well as pore collapse during compression. Specifically, in concrete materials, deviatoric deformation (represented here in rate form by  $\hat{\mathbf{L}}^D$ ) consists of micro-cracking, frictional crack sliding, rubble formation, and eventual granular flow [12,15,59]. Such irreversible deformation modes typically initiate at weak links in the microstructure such as aggregate–mortar interfaces, but may also occur alongside mortar fissures and aggregate cracking at large deformations [4,19]. Let  $\omega$  represent the cumulative local micro-cracked area per unit intermediate volume, such that  $D = \omega / \omega_c$ , where  $\omega_c$  is a material parameter denoting the maximum sustainable crack density, subject to the restriction  $0 \leq D \leq 1$ . This is

a modeling assumption unique to the present theory, providing a simple linear relationship between crack density, a micromechanical quantity, and damage  $D$ , a macroscopic continuum quantity. When the material is undamaged, the crack density is assumed negligible ( $\omega = 0$ ), while the crack density achieves its maximum value ( $\omega = \omega_c$ ) when catastrophic failure of the material element occurs, e.g., micro-crack percolation. Perhaps most ideally, the property  $\omega_c$  could be determined from microscopic investigations, including data obtained from micromechanical experiments and/or computations, of concrete microstructures undergoing dynamic fracture and fragmentation. However, such microscopic data are presently unavailable for the material of study in the simulations that follow. Instead,  $\omega_c$  is chosen for concrete following the experimental observation that typical fragments are of a size commensurate with that of the aggregate, as discussed in detail later in Section 4. Such an approach, with micromechanically inspired constants determined from macroscopic data, is common in practice [29]. Though the model presented here suffices for the present investigation, more realistic relationships between damage and microstructure could be envisioned, at the expense of additional experiments needed to determine any added parameters.

The specific free energy density is postulated on a per unit intermediate configuration volume basis as

$$\tilde{\rho}\psi = K(\vartheta_E, \varphi)\vartheta_E^2 + G(1 - D)\hat{\mathbf{E}}^E : \hat{\mathbf{E}}^E + \Gamma(D) + Y(\theta), \quad (14)$$

where the intermediate mass density  $\tilde{\rho} = \rho J^E$ ,  $K$  is the effective bulk modulus,  $G$  is the shear modulus of the undamaged material,  $\hat{\mathbf{E}}^E = \mathbf{E}^E - (\vartheta_E/3)\mathbf{1}$  is the elastic strain deviator,  $\Gamma$  accounts for surface and concentrated elastic energy in the vicinity of micro-cracks, and  $Y$  describes the specific heat content. The bulk modulus takes the particular form

$$K = K_E(\varphi_L - \varphi)/(2\varphi_L) + (K_1/2 + K_2\vartheta_E/3 + K_3\vartheta_E^2/4)(\varphi/\varphi_L), \quad (15)$$

where  $K_E$  is the elastic bulk modulus of the initially porous material, the parameter  $\varphi_L$  denotes the maximum porosity reduction due to compressive pressure loading, and  $K_1$ ,  $K_2$ , and  $K_3$  determine the pressure–volume relationship for fully dense material at  $\varphi = \varphi_L$ . The micro-crack energy per unit intermediate volume is written as

$$-\Gamma = \gamma\omega = (K_C^2\omega_c D)/(2K_E), \quad (16)$$

where  $\gamma = K_C^2/2K_E$  is the surface energy of fracture [49], with  $K_C$  the effective fracture toughness. The negative sign denotes internal energy release (positive dissipation) upon fracture. As will be discussed later, the stored micro-elastic energy released in (16) is assumed to contribute to the continuum energy balance (13) only until fragmentation commences, following which the energy dissipated is converted to local kinetic energy of fragment expansion.

The intermediate second Piola–Kirchhoff stress is defined by

$$\mathbf{S} = \tilde{\rho} \frac{\partial \psi}{\partial \mathbf{E}^E} = J^E \mathbf{F}^{E-1} \boldsymbol{\sigma} \mathbf{F}^{E-T}. \quad (17)$$

From (14) and (15), hydrostatic and deviatoric parts of  $\mathbf{S}$  are then found as

$$\begin{aligned} \tilde{p} &= -\text{tr} \mathbf{S}/3 \\ &= -K_E \vartheta_E (\varphi_L - \varphi)/\varphi_L - (K_1 \vartheta_E + K_2 \vartheta_E^2 + K_3 \vartheta_E^3) \varphi/\varphi_L, \end{aligned} \quad (18)$$

$$\hat{\mathbf{S}} = \mathbf{S} + \tilde{p}\mathbf{1} = 2(1 - D)G\hat{\mathbf{E}}^E. \quad (19)$$

The Cauchy pressure is  $-3p = \text{tr} \boldsymbol{\sigma} = \text{tr}(J^{E-1} \mathbf{F}^E \mathbf{S} \mathbf{F}^{E-T})$ .

Deviatoric plastic deformation follows from the flow potential  $\Phi$ , which is equated here with the effective deviatoric stress  $\hat{\boldsymbol{\sigma}} = \sqrt{(\frac{2}{3})\hat{\boldsymbol{\sigma}} : \hat{\boldsymbol{\sigma}}}$ :

$$\begin{aligned} \hat{\mathbf{L}}^D &= \lambda \frac{\partial \Phi}{\partial \hat{\boldsymbol{\sigma}}}, \\ \Phi &= [\bar{A}(1 - D) + \bar{B}(p/\sigma_0)^{\bar{N}}] \\ &\quad \times [1 + \bar{C} \ln(\hat{\boldsymbol{\epsilon}}/\hat{\boldsymbol{\epsilon}}_0)] \sigma_0 \quad (p/\sigma_0 > -\bar{T}), \end{aligned} \quad (20)$$

where  $3\lambda^2 = 2\hat{\mathbf{L}}^D : \hat{\mathbf{L}}^D$  for stresses exceeding the elastic limit,  $\hat{\boldsymbol{\sigma}}$  is the deviatoric stress,  $\hat{\boldsymbol{\epsilon}} = \sqrt{(\frac{2}{3})\hat{\mathbf{D}} : \hat{\mathbf{D}}}$  (with  $\hat{\mathbf{D}}$  the symmetric deviatoric part of  $\mathbf{L}$ ), and  $\bar{A}$ ,  $\bar{B}$ ,  $\bar{C}$ ,  $\bar{N}$ ,  $\hat{\boldsymbol{\epsilon}}_0$ , and  $\sigma_0$  are material parameters.  $\bar{T}$  is equivalent to the ratio  $-\tilde{p}/\sigma_0$ , with  $\tilde{p}$  the tensile pressure at failure. Note that the flow potential used in (20) is identical to that of the HJC model [7].

In the present implementation, an isotropic inelastic response is assumed such that the inelastic spin may be neglected, as indicated by  $\mathbf{L}^D = \mathbf{L}^{DT}$ . Furthermore, note that  $\mathbf{L}^D \approx \hat{\mathbf{F}}^D \mathbf{F}^{D-1}$  when elastic shape changes are small, an assumption made later in the numerical implementation to facilitate solution of large problems. The null plastic spin assumption is standard for isotropic materials [60]. With this assumption, the flow rule in the first of (20), written in terms of the effective deviatoric stress, is of a form consistent with the historic plasticity literature [61].

Porosity and damage evolution are controlled via the kinetic relations

$$\begin{aligned} \dot{\varphi} &= \begin{cases} 0 & (p \leq p_C; p \geq p_L), \\ \hat{\alpha} \langle \tilde{p} \rangle / \sigma_0 & (p_C < p < p_L), \end{cases} \\ \dot{D} &= \hat{\kappa} \lambda (1 - \pi_D(p/\sigma_0)) + \bar{T}^{-1} \langle -\dot{p} / \sigma_0 \rangle, \end{aligned} \quad (21)$$

where  $\hat{\alpha}$ ,  $\hat{\kappa}$ , and  $\pi_D$  are positive constants, and the bracket notation  $2\langle x \rangle = x + |x|$ . The pressure at which inelastic crushing commences is denoted by  $p_C$ , and the locking pressure corresponding to  $\varphi_L$  is denoted as  $p_L$ . Notice from (21) that both  $\dot{\varphi}$  and  $\dot{D}$  are always positive, i.e., irreversible. Note that although the particular forms of Eqs. (21) may be new, these are differential equations of a rate form typically encountered in internal state variable theories [33].

The physical interpretation and motivation for (21) is as follows. At compressive pressures lower than  $p_C$ , volumetric deformation is assumed elastic and pore collapse does not occur. On the other hand, when pressures exceed  $p_L$ , all pores have been compressed and the material is fully dense. Finally, at pressures between crushing ( $p_C$ ) and locking ( $p_L$ ), a linear relationship is implied between changes in pressure and pore compaction. Damage in the form of micro-cracking evolves in conjunction with inelastic deformation  $\lambda = \sqrt{\frac{2}{3}} \hat{\mathbf{L}}^D : \hat{\mathbf{L}}^D$ , since inelastic deformation is assumed to consist of matrix–aggregate separation and micro-crack sliding. Increases in tensile pressure ( $p < 0$ ) further exacerbate the initiation and growth of cracks in the microstructure [59]. It is noted that (21) has been developed for describing dynamic failure events, such as spall and fragmentation upon ballistic impact, and may not reproduce details of rubble formation and localized deformation modes such as cone and shear failures occurring during static unconfined compression [4], for example.

The model is next evaluated in terms of thermodynamic admissibility. From (14)–(16),

$$-\rho \frac{\partial \psi}{\partial D} = J^{E-1} \left( G \hat{\mathbf{E}}^E : \hat{\mathbf{E}}^E + \frac{K_C^2 \omega_C}{2K_E} \right), \quad (22)$$

$$-\rho \frac{\partial \psi}{\partial \varphi} = J^{E-1} [\rho_0 \psi + K_E \vartheta_E^2 / (2\varphi_L) - (K_1/2 + K_2 \vartheta_E/3 + K_3 \vartheta_E^2/4)(\vartheta_E^2/\varphi_L)]. \quad (23)$$

Returning to (11), now consider the strong form of the second law:

$$\boldsymbol{\sigma} : \hat{\mathbf{L}}^D - \rho \frac{\partial \psi}{\partial D} \dot{D} + \left( \frac{p}{1+\varphi} - \rho \frac{\partial \psi}{\partial \varphi} \right) \dot{\varphi} \geq 0, \quad (24)$$

$$-\mathbf{q} \cdot \partial_x \theta \geq 0.$$

Using (20) and (21),

$$\hat{\boldsymbol{\sigma}} : \hat{\mathbf{L}}^D = \lambda \hat{\boldsymbol{\sigma}} : \frac{\partial \Phi}{\partial \hat{\boldsymbol{\sigma}}} = \frac{\lambda}{2\bar{\sigma}} \hat{\boldsymbol{\sigma}} : \hat{\boldsymbol{\sigma}} \geq 0, \quad (25)$$

$$-J^E \rho \frac{\partial \psi}{\partial D} \dot{D} = \left[ \frac{(\varphi_L - \varphi)}{2\varphi_L} K_E \vartheta_E^2 + G \hat{\mathbf{E}}^E : \hat{\mathbf{E}}^E + \frac{K_C^2 \omega_C}{2K_E} \right] \times [\hat{\kappa} \lambda \langle 1 - \pi_D(p/\sigma_0) \rangle + \bar{T}^{-1} \langle \dot{p}/\sigma_0 \rangle] \geq 0, \quad (26)$$

meaning that the kinetic relations for plastic flow (20) and damage evolution (21) are consistent with the laws of thermodynamics in (7), (8), and (24). Note also that a different flow potential  $\Phi$  could be used in (20) should a more complex yield surface be necessary, for example capturing anisotropy, creep, or cyclic loading [15–18]. The energy dissipated in (25) corresponds physically to irreversible processes associated with micro-crack sliding and frictional granular flow mechanisms, contributing mainly to temperature rise in (13) under near-adiabatic conditions. So long as (25) is satisfied, thermodynamic admissibility of the plasticity component of the model

framework is maintained. For evolution of porosity, the following constraint emerges in terms of the pressure, considering (23), as  $\dot{\varphi} \geq 0$  from the first of (21):

$$p \geq \frac{(1 + \varphi_L)}{J^E \varphi_L} (K_1/2 + K_2 \vartheta_E/3 + K_3 \vartheta_E^2/4) \vartheta_E^2 = A. \quad (27)$$

Subsequently, material parameters are selected such that (27) is satisfied over the range of applicability of the model.

Similarities between the present approach and existing models are clarified in the discussion that follows. Some features of the model developed here are shared with HJC model of [7]. As will be demonstrated later, the EPIC (2003 version) computational platform was used for the large scale simulations, and the built-in HJC model of that code was used as a guide for developing some aspects of the present constitutive model. To this end, the authors of [7,62] are commended for providing clear documentation and references used in the determination of material constants of the very same composition of concrete (SAC-7) of interest in the simulations that follow in the present study. Likewise the software developers are acknowledged for supplying an efficient, manageable, and portable code that provided robust algorithms for element-to-particle conversion [46,47] essential for capturing fragment debris in the simulations to be discussed later. Specifically, here the same plastic flow potential in (20), and corresponding plasticity parameters (see later Table 1) are used verbatim from [7]. However, the porosity equation is written in rate form (21) as opposed to a monotonic algebraic relationship between pressure and specific volume used in [7]. Furthermore, the damage evolution equation is written in rate form in (21), as opposed to the incremental form based on cumulative plastic and volumetric strain increments used in [7]. Rate forms were used here to satisfy the thermodynamics of (13) and (24), which are not transparently compatible with kinetic equations based on cumulative strain increments. It is noted that the experimental data given in [7] and references therein [6,63,64] were used to develop these relationships and select parameters, as will be discussed in more detail in Section 4. For this reason, stress–strain behaviors predicted by the present theory and the HJC model are similar for uniaxial stress states, especially prior to the accumulation of significant damage. However, it is noted in [7] that the constants for plasticity and damage evolution may not have been determined uniquely in the HJC model due to lack of experimental data over a complete range of pressures and strain rates; the same limitations apply here. For this reason, and for the different forms of the evolution equations (20), the failure behavior predicted by the present theory and that of [7] will be different for arbitrarily general stress histories.

Other differences between the present constitutive model and that of [7] are now listed. The HJC model relies on an additive split of the velocity gradient into elastic and inelastic parts, as opposed to the multiplicative kinematics of (1). Further, in the HJC engineering model, no strain

Table 1  
Model parameters for SAC-7 (48 MPa) concrete

Constant	Value	Description
$\rho_0$	2440 kg/m <sup>3</sup>	Reference mass density <sup>a</sup>
$\kappa$	1.76 W/(m K)	Thermal conductivity <sup>a</sup>
$\hat{c}$	654 J/(kg K)	Specific heat capacity <sup>a</sup>
$K_E$	15.9 GPa	Initial elastic bulk modulus <sup>a</sup>
$K_1$	85.0 GPa	Compressed first order bulk modulus
$K_2$	−151 GPa	Compressed second order bulk modulus
$K_3$	208 GPa	Compressed third order bulk modulus
$\hat{K}_2$	−171 GPa	Modified second order bulk modulus <sup>a</sup> ( $p \gg p_L$ )
$G$	14.9 GPa	Shear modulus <sup>a</sup>
$\varphi_L$	0.10	Maximum porosity reduction <sup>a</sup>
$p_C$	0.016	Threshold pressure for irreversible crushing <sup>a</sup>
$p_L$	0.080 GPa	Pressure at maximum porosity reduction <sup>a</sup>
$\bar{A}$	0.79	HJC strength parameter <sup>a</sup>
$\bar{B}$	1.60	HJC pressure parameter <sup>a</sup>
$\bar{C}$	0.007	HJC strain rate parameter <sup>a</sup>
$\bar{N}$	0.61	HJC pressure exponent <sup>a</sup>
$\dot{\epsilon}_0$	1.0/s	Reference strain rate <sup>a</sup>
$\sigma_0$	0.048 GPa	Static compressive yield strength <sup>a</sup>
$\bar{T}$	0.083	Maximum allowable tensile pressure <sup>a</sup>
$K_C$	0.831 MPa m <sup>1/2</sup>	Fracture toughness
$\omega_C$	1.7(10 <sup>5</sup> )m <sup>−1</sup>	Maximum crack density ( $\omega$ at $D = 1$ )
$\hat{\alpha}$	0.00614	Porosity evolution parameter
$\hat{\kappa}$	300	Damage evolution parameter
$\pi_D$	4.00	Damage evolution parameter
$D_T$	0.50	Threshold damage for fragmentation initiation

<sup>a</sup>Denotes parameter obtained or derived from Ref. [7].

energy function is given from which the elastic moduli are derived. Instead, piecewise linear and nonlinear relations are given for the bulk modulus, fit to the data of [6]. Modifications to the shear modulus upon damage accumulation or porosity compaction are not discussed in the original paper [7]. On the other hand, here a free energy function is postulated explicitly in (14), from which the elasticity relations are derived naturally in (10), (15), and (17)–(19). Here, the Green elastic strain (5) is used in the free energy (9) as an independent constitutive variable, consistent with other accepted theories of finite deformation thermo-mechanics [23,24,34].

The shear modulus is reduced linearly with increasing damage  $D$  in (14) and (19), inspired from simple damage mechanics-based arguments relating effective moduli with micro-crack densities [26–28]. In the HJC theory [7], no connection between  $D$  and micro-cracks is made. However the assumption made here, relating  $D$  to micro-crack density, is not necessarily inconsistent with the yield surface (20) formulated in [7]. Furthermore, the prescription of linearly decreasing deviatoric inelastic strength in (20) with increasing  $D$  is consistent with the analogous reduction in shear modulus with increasing  $D$  in the present theory.

Also, in (15) the effective bulk modulus is interpolated linearly between elastic ( $K_E$ ) value at null compression and the cubic Hugoniot curve at full compaction. In the present framework, the bulk modulus is not reduced upon accumulation of damage  $D$ , but such an effect could be

incorporated to reflect damage-induced losses in volumetric elastic stiffness under tensile stress states. It is noted that similar pressure–volume responses are predicted between the present theory and the HJC model [7] for a particular composition of concrete, since both are fitted to the same triaxial compression data [6].

A fundamental difference of the present theory with many others [7,12,15–18] is the present model’s explicit tracking of internal energy changes due to evolution of damage  $D$  in the constitutive theory. The fracture energy  $\Gamma$  in (14) and (16) accounts for the local elastic energy released by breaking bonds during micro-crack initiation and extension. This energy is distinct from that dissipated during plastic deformation in (25), e.g., crack sliding and granular flow contributing to frictional heating. However, both dissipative mechanisms tend to occur simultaneously, as damage growth is driven by plastic flow via (21), except for cases wherein the compressive pressure provides enough confinement to suppress increases in  $D$  in the constitutive model. As will be discussed later in Section 3, this fracture energy provides a counterbalance to the expansion kinetic energy that drives the fragmentation process (under the same deformation conditions, the greater the fracture energy, the fewer fragments produced per unit mass). Such an effect, whereby the energy dissipated due to damage evolution in the bulk constitutive model is explicitly transferred to fuel the formation of fragment debris, has not been emphasized elsewhere. In particular, the HJC model [7] does not at present incorporate any means for computing fragment sizes, though some post-processing capabilities exist in the EPIC code for metals [35]. Also, no connection between  $D$  and crack energy is made in the HJC model [7].

Tangible benefits arise from formulating a finite deformation constitutive theory that explicitly accounts for restrictions imposed by the laws of thermodynamics, as opposed to a purely mechanical model that may appear more simple and tractable for general engineering practice. When selecting parameters and constitutive equations, non-physical behavior can be avoided if thermodynamic restrictions on dissipation are addressed [65]. Irreversible processes such as damage accumulation, internal friction, and inelastic deformation should cause energy dissipation, as opposed to energy storage, in the material [16]. Incorrect estimates of energy dissipation could lead to inaccurate temperature predictions in high rate simulations of material behavior, when conditions may be nearly adiabatic. Effects of temperature on the mechanical response will be greatest if the elastic constants, pressure, and/or flow stress depend explicitly on temperature. They do not here, but such temperature effects could be incorporated later into the present theory when data become available, and such effects are thought to be important for crushable materials subjected to shock loading [32].

The value of the present general theory may be more fully realized as it is extended to other materials. For example, finite deformation elasticity may be even more

useful for describing those materials, such as crystalline ceramics, that undergo little plasticity or inelastic volume change under shock loading. The connection of damage variable  $D$  to micro-crack density provides an opportunity for computational and experimental micromechanics [28,56] to provide a physical basis for damage evolution equations and parameters.

While the theory appears complex, it is emphasized that the inequalities entering the thermodynamic analysis in (24)–(27) need not be consulted once the kinetic equations and corresponding parameters have been chosen for a particular material. It is also noted that the number of parameters in the present theory is not excessive, with only a few more needed here than in [7] for example, specifically in order to address fracture energy and fragmentation. Furthermore, in the large scale computations to be discussed later, much of the execution time is apparently consumed by particle neighbor search algorithms, as opposed to the constitutive update of the material response.

### 3. Fragmentation modeling

Two methods for describing fragment size and velocity statistics are developed here. The first method, termed the ‘energetic approach’, relies on a local energy balance to compute the fragment size and number of fragment(s) associated with each local volume element (e.g., a finite element, computational cell, or particle in a numerical scheme), and assigns to all fragment(s) the local velocity of that volume element. The second method, termed the ‘statistical physics approach’, is derived upon maximization of a global statistical entropy function subject to constraints regarding conservation of mass, energy, and momentum.

#### 3.1. Energetic approach

Fragmentation of the local volume element is assumed to occur over a (small) time period, beginning when the damage reaches a threshold value,  $D = D_T$ . Over this period, the energy released per unit volume due to internal micro-cracking is estimated, from (16), as

$$\begin{aligned} \rho e_D &= \int_{D_T}^D [K_C^2 \omega_C / (2K_E)] dD \\ &= K_C^2 \omega_C (D - D_T) / (2K_E). \end{aligned} \quad (28)$$

During the fragmentation process, the material is assumed to retain all energy apart from  $e_D$ , which may be stored via (14) or dissipated as heat. Prior to fragmentation,  $\Gamma$  contributes to the dissipation and possible temperature rise via (13) and (26); then, upon  $D = D_T$ , this energy contributes to the relative kinetic energy of fragments. Instantaneous energy transfer from fracture to fragmentation follows from

$$M \dot{e}_D = M \rho^{-1} \dot{\Gamma} |_{D \geq D_T} = d \sum (u_l + u_s) / dt, \quad (29)$$

where  $M$  is the total mass of the volume element, and  $u_l$  and  $u_s$  denote absolute energies due to the relative linear and spin momenta per fragment. Note that these energies are distinct from the kinetic energy of translation and rotation of the center of mass of the element, which are assumed to be conserved during the fragmentation process. Summation in (29) is implied over all fragments comprising the particular volume element under consideration.

Assuming cube-shaped fragments with edge length  $b$ , energies can be estimated as

$$u_l = b^5 \rho \dot{\epsilon}^2 / 16, \quad u_s = b^5 \rho \dot{\phi}^2 / 12, \quad (30)$$

where the effective strain rate in the fragment is  $\dot{\epsilon} = \sqrt{\mathbf{D} : \mathbf{D}}$ , with  $\mathbf{D}$  the symmetric part of  $\mathbf{L}$ , and  $\dot{\phi}$  is the rate of rotation of the fragment about its moment of inertia. The velocity gradient  $\mathbf{L}$  is assumed to be distributed uniformly over the fragment population comprising the continuum volume element, equivalent to the global value assigned to that element [35]. Combining (29) and (30),

$$\left( \sum \rho b^3 \right) \dot{e}_D = \frac{d}{dt} \sum (b^5 \rho \dot{\epsilon}^2 / 16 + b^5 \rho \dot{\phi}^2 / 12). \quad (31)$$

Assuming that the mass density is equal and constant among  $N$  fragments, replacing  $b$  with a mean effective length  $\bar{b}^3 = (\rho N)^{-1} M$ , and integrating with respect to time, (31) becomes

$$\bar{b} = \sqrt{\frac{8K_C^2 \omega_C (D - D_T)}{K_E \rho (\dot{\epsilon})^2}}, \quad (32)$$

where the rotation  $\dot{\phi}$  has been omitted in (32), as the translational energy is assumed here to far exceed the rotational energy of the fragments, and since rotation rates of fragments are difficult to quantify from experimental observations [58] modeled later. Equation (32) yields the mean fragment dimension  $\bar{b}$ . Mass conservation then provides the local number of fragments  $N = M / (\rho \bar{b}^3)$ . Note that (32) is a time-integrated generalization of the energy rate balance (31); as a result, the mean fragment dimension is inversely proportional to the strain rate in (32), and not the second time derivative of strain.

Equation (32) may be written in the alternative form

$$\bar{b} = \hat{A} [K_C^2 / (K_E \rho \dot{\epsilon}^2)]^{\hat{N}}, \quad (33)$$

where  $\hat{A} = 2.83 \sqrt{\omega_C (D - D_T)}$  and  $\hat{N} = \frac{1}{2}$ . This can be compared with the brittle fragmentation model of Grady [48], in which  $\hat{A} = 2.71$  and  $\hat{N} = \frac{1}{3}$ , and the ductile failure model of Johnson and Cook [35], which exhibits the form of (33) with the substitutions  $\hat{A} = 4$ ,  $\hat{N} = \frac{1}{2}$ , and  $K_C^2 = K_E \bar{\sigma} \bar{\epsilon}$ . All models predict a decrease in mean fragment dimension with increasing strain rate, in agreement with general observations on dynamically fragmenting solids [49]. Decreasing fragment sizes with increasing strain rate have been predicted elsewhere specifically for concrete and mortar [66].

Note that the derivation of (32) follows from the assumption that the expansion kinetic energy of the

fragments balances the fracture energy of the material; similar assumptions have been made elsewhere with minor variations, most notably [35,48–51]. The theory leads to the logical conclusion that the more rapidly a mass of material is straining or deforming, the more fragments it will produce. The use of effective strain rates generalizes derivations based on spherical expansion or 1D failure [48–50]. The angular rotation rate of the fragments is neglected in the applications that follow in the present work, though such rotations could logically derive from the spin of the continuum material. For example, analogously to the definition of  $\dot{\epsilon}$ , one may assume that  $\dot{\phi} = |\dot{\epsilon} : \mathbf{W}|$ , where  $\mathbf{W}$  is the skew part of  $\mathbf{L}$ , and  $\epsilon$  is the rank 3 permutation tensor.

The new contribution here is introduction of parameters  $D_T$  and  $\omega_C$  into the fragment size expression (32). The former introduces history effects in a simple manner: only the strain rate  $\dot{\epsilon}$  that occurs during the fragmentation process, when  $D > D_T$ , is used in the computation of the fragment size, as is discussed in more detail in Section 4. This prevents fragments from forming during processes in which the material undergoes no damage, for example during purely elastic deformation. The use of  $\omega_C$  connects the fragmentation energy consumed during dynamic expansion with the fracture energy resulting from damage evolution in the bulk constitutive model.

A common approach involves only post-processing calculations to determine fragment sizes, with the average strain rate over the entire history of the problem considered [35]. In such an approach, the fragmentation energy does not influence the constitutive response of the bulk material. On the other hand, here the fragmentation event influences the bulk response and vice versa through the exchange of energy, from damage dissipation to fragment expansion, as discussed following Eq. (28) and illustrated in Fig. 1. In general, theories such as [35,48–51] are based on an energy balance or energy minimization and are consistent with thermodynamic principles. However, implementation of such models in a purely post-processing capacity, irrespective of how the fragmentation energy is supplied or extracted from the bulk constitutive model, may not, in principle, properly account for the energy consumed during frag-

mentation. It is noted, however, that such energy exchanged during fragmentation may be negligible compared to that induced by plastic dissipation, and that material elements undergoing significant damage accumulation tend to support little mechanical strength, so such a non-physical assumption may present few difficulties in practical computations.

### 3.2. Statistical physics approach

Here, the entire fragmenting body is considered at once, and it remains to be determined how the masses and velocities are distributed among fragments comprising this body. The issue is resolved upon consideration of entropy maximization constrained by mass, momentum, and energy conservation. In what follows, fragment mass and velocity distributions are derived individually, then combined to form a joint probability function capturing both fragment sizes and speeds.

The mass distribution follows from entropy maximization subjected to the constraints that the total mass and total number of fragments are known, following a procedure outlined by Grady and Kipp [53]. These constraints are written as

$$M = \rho \sum b^3 = \rho N \bar{b}^3, \tag{34}$$

where it is assumed that the density is the same among all fragments and the velocity does not affect the mass distribution, and  $M$  and  $\bar{b}$  are known from mass conservation and a global application of the preceding energetic analysis, respectively. A measure of the statistical entropy associated with the mass distribution is  $S_M = k_B \ln P$ , where  $k_B$  is Boltzmann’s constant and  $P$  is the number of possible fragment arrangements. The value of  $S_M$  is maximized by maximizing the quantity [67]

$$\ln P = N \ln N - \sum_{i=0}^j n_i \ln n_i, \tag{35}$$

where  $n_i$  is the number of fragments of mass  $m_i \leq m < m_i + \delta m_i$ , with  $\delta m_i$  describing the range of masses admitted in each bin  $i$ , and with  $j$  the total number of bins. In (35) it is implicitly assumed that  $n_i$  are large numbers.

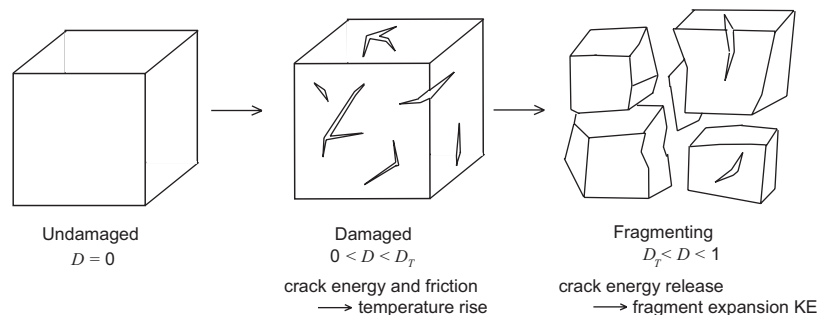


Fig. 1. Damage evolution and fragmentation process.

Constraints (34) are rewritten simply as

$$N = \sum_{i=0}^j n_i, \quad M = \sum_{i=0}^j m_i. \quad (36)$$

Introducing Lagrange multipliers  $\alpha$  and  $\beta$ , an equivalent function  $f(n_i)$  is defined as

$$f = \ln P + \alpha \left( N - \sum n_i \right) + \beta \left( M - \sum m_i \right), \quad (37)$$

which is maximized via the solution of

$$\frac{\partial f}{\partial n_i} = -(1 + \ln n_i) - \alpha - \beta m_i = 0. \quad (38)$$

Making the notation change  $\alpha + 1 \rightarrow \alpha$ , (38) yields

$$n_i = \exp(-\alpha - \beta m_i). \quad (39)$$

Rewriting (36) as integrals of continuous functions [53],

$$\begin{aligned} N &= \int_0^\infty n \, dm = \int_0^\infty \exp(-\alpha - \beta m) \, dm \\ &= \exp(-\alpha)/\beta, \end{aligned} \quad (40)$$

$$\begin{aligned} M &= \int_0^\infty mn \, dm = \int_0^\infty m \exp(-\alpha - \beta m) \, dm \\ &= \exp(-\alpha)/\beta^2. \end{aligned} \quad (41)$$

Finally, (39) becomes

$$\hat{n}(m_i) = n_i = (N^2/M) \exp(-Nm_i/M), \quad (42)$$

with the cumulative probability distribution of fragments larger than  $m$  given by

$$\hat{n}(m)/N = N_0 \exp(-N_0 m), \quad (43)$$

where  $N_0 M = N$ .

The fragment velocity distribution follows from similar arguments. A measure of the statistical entropy associated with the velocity distribution is  $S_V = k_B \ln W$ , attaining its greatest value upon maximization of the function

$$\ln W = N \ln N - \sum_{i=0}^j n_i \ln n_i, \quad (44)$$

where  $n_i$  is the number of fragments with kinetic energy  $e_i \leq e < e_i + \delta e_i$ , with  $\delta e_i$  spanning the range of energies admitted in each bin  $i$ . The constraints on the distribution are written as

$$N = \sum_{i=0}^j n_i, \quad E = \sum_{i=0}^j e_i, \quad (45)$$

where  $E$  is the total kinetic energy of the fragment cloud that will be determined later. Following an analogous procedure to that in (37)–(38),

$$n_i = \exp(-\alpha - \beta e_i), \quad (46)$$

where the Lagrange multipliers  $\alpha$  and  $\beta$  are determined as follows. Making the analogy with rigid molecules [67], let

$$\beta = 1/(k_B T) = (3N)/(2E), \quad (47)$$

where  $T$  is a thermodynamic temperature. Then

$$n_i = \exp[-\alpha - (3Ne_i)/(2E)]. \quad (48)$$

Assume that in ballistic scenarios the fragment velocity is unidirectional, coaxial with the velocity of the center of mass of the fragment cloud, such that  $2e_i = m_i v_i^2$ . Then the probability distribution is

$$\hat{n}(v_i) = A \exp[(-3Nm_i v_i^2)/(4E)], \quad (49)$$

where  $A = \exp(-\alpha)$  is determined by normalization:

$$\begin{aligned} 1 &= \int_0^\infty \hat{n}(v) \, dv = A \int_0^\infty \exp[(-3Nm v^2)/(4E)] \, dv \\ &= A \sqrt{(\pi E)/(3mN)}, \end{aligned} \quad (50)$$

giving

$$\hat{n}(v) = \sqrt{(3mN)/(\pi E)} \exp[(-3Nm v^2)/(4E)]. \quad (51)$$

The form (51) differs from the velocity distribution obtained by Grady and Winfree [57], who assumed that the fragments may scatter randomly in three dimensions, yielding 3D Maxwell–Boltzmann-type velocity statistics. In the ballistic concrete perforation experiment that is described and simulated later, the flying debris tend to follow a roughly uni-directional path, with fragments enclosed in a cone angle of less than  $45^\circ$ , as opposed to a path of fully radial expansion.

The joint probability distribution of mass and velocity is derived by combining (43) and (51):

$$\begin{aligned} \hat{p}(m, v) &= \hat{n}(m)\hat{n}(v) \\ &= \sqrt{\frac{3mN^5}{\pi EM^2}} \exp \left[ -m \left( \frac{N}{M} + \frac{3N}{4E} v^2 \right) \right]. \end{aligned} \quad (52)$$

The following relations then arise for total probability, total fragment mass, mean velocity, and total linear momentum:

$$\int_0^\infty \int_0^\infty \hat{p}(m, v) \, dm \, dv = 1, \quad (53)$$

$$\begin{aligned} \int_0^\infty \int_0^\infty \hat{p}(m, v) m \, dm \, dv \\ = \int_0^\infty m \hat{n}(m) \left( \int_0^\infty \hat{n}(v) \, dv \right) \, dm = M, \end{aligned} \quad (54)$$

$$\begin{aligned} \frac{1}{N} \int_0^\infty \int_0^\infty \hat{p}(m, v) v \, dm \, dv \\ = \frac{1}{N} \int_0^\infty \hat{n}(m) \left( \int_0^\infty \hat{n}(v) v \, dv \right) \, dm = \sqrt{\frac{4E}{3M}}, \end{aligned} \quad (55)$$

$$\begin{aligned} \int_0^\infty \int_0^\infty \hat{p}(m, v) m v \, dm \, dv \\ = \int_0^\infty m \hat{n}(m) \left( \int_0^\infty \hat{n}(v) v \, dv \right) \, dm = \sqrt{EM/3}. \end{aligned} \quad (56)$$

Identifying (56) with the linear momentum of the fragment distribution, conservation of linear momentum demands

that the energy distributed to feed the velocity probability distribution is

$$E = 3\rho\bar{b}^3 N\bar{v}^2. \quad (57)$$

The mean velocity in (55) then becomes  $2\bar{v}$ , i.e., twice the velocity of the center of mass of the fragmenting body. The expansion energy of (28) does not contribute to the velocity distribution because this energy is consumed by the strain rate of the fragments as given by Eq. (30), as opposed to their linear velocities.

The method presented above, based on global entropy maximization, is offered as an alternative to the local energy balance method derived in Section 3.1. The second method provides a basis for comparison of numerical results in the absence of quantitative data on fragment velocities, which are scarce for materials of present interest. The differences between the two approaches are as follows. For the approach in Section 3.1, a local energy balance leads to a local fragment dimension. In the numerical implementation to be discussed later in Section 4, each particle is then assigned its own number of fragments, with the size of these based on the local strain rate history and damage evolution in that particle (or corresponding element). Consideration of all particles then provides statistical distributions of fragment mass and velocity, with velocities of fragments obtained directly from parent particles. In contrast, in the statistical method of the present section, distributions of fragment sizes and velocities are found using (52), irrespective of the local particles' velocities and the masses associated with each; only the total fragment mass and kinetic energy are needed (these are supplied by the computation). In this way, distributional information is provided by the universal entropy maximization procedure in lieu of the local physics from the constitutive update and particle algorithms. This tends to make the statistics-based method less sensitive to the meshes used in the computations, as will be demonstrated in Section 5.1, though the sensitivity of the former energetic approach to mesh density is not excessive here. Both methods are motivated by and address principles of mass, energy, and momentum conservation. The new contribution in the present section is derivation of the joint mass–velocity distribution (52) in the context of 1D fragment trajectories, and derivation of Eq. (57), the energy fueling the fragment velocities, neither of which was given explicitly in [57].

It is noted that geometry-based fragmentation theories, such as discussed in [52,53], are often not developed via direct thermodynamic considerations. However, this does not mean such models contradict thermodynamic principles, and in fact, many have been analyzed and justified using entropy methods from statistical mechanics [54–57]. So long as the energy consumed during damage and fragmentation is tracked correctly in the constitutive model, it is thought here that such approaches are reasonable from a thermodynamic perspective. In the

problems considered later in Section 5, calculations accessing the constitutive model are needed to supply global data—specifically the collective mass, number, and linear momentum—entering the statistical theory to produce the distributions of mass and velocity, which in turn satisfy global conservation laws via (53)–(57). Though unlikely, if such data are known a priori from experimental or analytical means, then the constitutive model and numerical simulations will not be needed for predicting fragmentation statistics with a single equation such as (52) or those in [52,53].

#### 4. Concrete material modeling

The model was applied here to study a particular concrete material. Properties, parameter selection, and numerical implementation are described briefly in what follows.

##### 4.1. Material properties and parameters

The preceding theory was applied to describe a concrete of unconfined compressive strength 48 MPa (7 ksi), as studied previously by Hanchak et al. [6] and Holmquist et al. [7]. Parameters are listed in Table 1.

Constants marked with a superscript were obtained from [7]; most of these enter the yield function (20). Note that our framework is general in the sense that an alternative—and possibly more robust for certain complex load histories—plastic potential for deviatoric flow could be substituted for  $\Phi$  and the HJC plasticity parameters entering Eq. (20) while still maintaining thermodynamic admissibility of the kinetic relations. Also, identical constants were often found to adequately address behavior for which elastic strains were small, such that differences in pressures  $\tilde{p}$  and  $p$  in intermediate and spatial frames, respectively, were negligible.

The fully crushed material is assumed to behave similarly to the aggregate at high pressures, following [7]. For this concrete, the aggregate is assumed to consist of fine- and coarse-grained granite stones [6]. Constants  $K_1$ ,  $K_2$ , and  $K_3$ , describing the volumetric elastic response of the fully crushed material, were determined by fitting the pressure–volume response of (18) to the shock Hugoniot data for granite [64], assuming purely volumetric elastic deformation of the form  $\mathbf{F}^E = (1 - \chi)\mathbf{1}$ . The fit, shown in Fig. 2, is deemed accurate for pressures up to 20 GPa. Porosity evolution parameter  $\hat{\alpha}$  was found from linear interpolation between crushing and locking pressures, i.e.,  $\hat{\alpha} = \varphi_L \sigma_0 / (p_L - p_C)$ . The pressure–volume response under triaxial loading at pressures under 20 GPa is shown in Fig. 3 and compared with experimental data [6]. Here,  $\mu = \rho / \rho_0 - 1$  is the total volumetric strain. The complete pressure–volume response and porosity change under triaxial compression are given in Fig. 4; notice the abrupt increase in effective bulk modulus upon attainment of the locking pressure, at which  $\varphi = \varphi_L$ . Thermodynamic

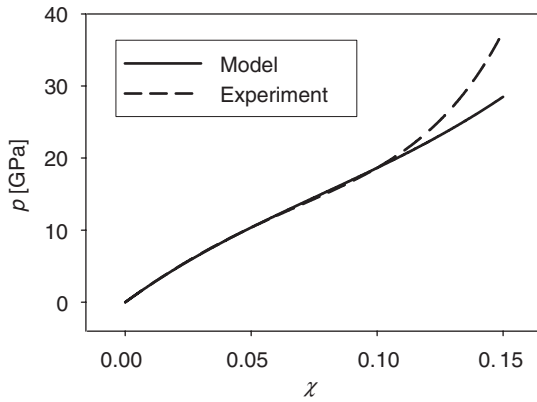


Fig. 2. Pressure  $p$  vs. elastic volumetric deformation  $\chi$ , fully crushed material (experimental data from [64]).

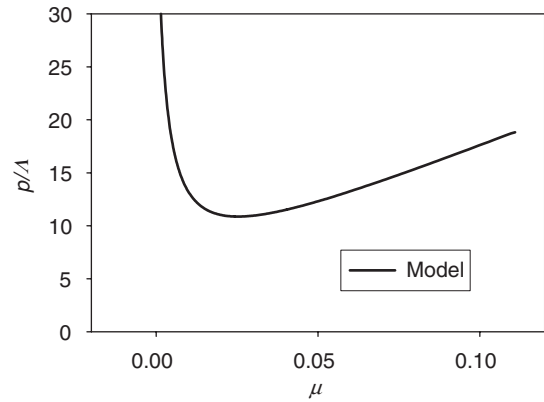


Fig. 5. Thermodynamic dissipation ratio associated with porosity evolution.

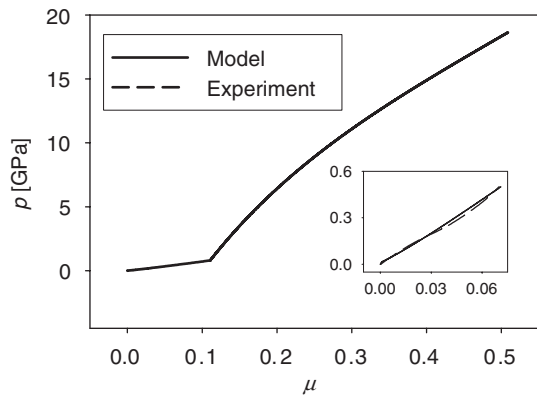


Fig. 3. Pressure  $p$  vs. volumetric deformation  $\mu$ , small compression range (experimental data from [3]).

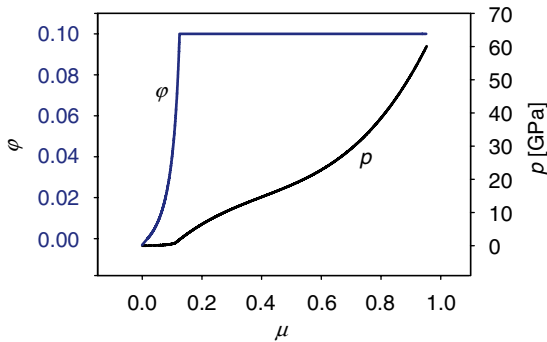


Fig. 4. Porosity compaction  $\phi$  and pressure  $p$  vs. volumetric deformation  $\mu$ , large compression range (model only).

admissibility of porosity evolution, from inequality (27), was verified for all  $\phi > 0$ , as shown in Fig. 5.

Fracture toughness  $K_C$  was obtained from [67] and was assumed constant. However, it is noted that variability in fracture strength is expected depending upon loading rate, stress state, specimen size, and composition [68]. Following monotonic and cyclic slow-rate test data and analyses given in [6,7,63], failure occurs ( $D = 1$ ) when the cumulative

plastic strain  $\lambda = 0.0033$  under null pressure conditions  $p/\sigma_0 = 0$ , giving  $\hat{k} = 300$ . Consulting the above references, prescribing  $D = 1$  when  $\lambda = 0.01$  under average pressure  $p/\sigma_0 = \frac{1}{6}$  yields  $\pi_D = 4$ .

The computed stress–strain responses for the concrete material deformed in uniaxial compression, tension, and shear are shown in Fig. 6. Results were obtained from deformation of a single dynamic finite element under conditions where imposed components of the deformation gradient  $F$  and nominal strain  $\epsilon$  were related as follows: for compression  $F_{11} = 1 - \epsilon$ , tension  $F_{11} = 1 + \epsilon$ , and shear  $F_{12} = \epsilon$ . The axial stress is plotted for tension/compression and the shear stress for shear deformation. Note that the material hardens slightly with strain rate, particularly in compression, in agreement with recent experiments [11]. The rate effect is less noticeable in pure shear, as the curves for rates  $\dot{\epsilon}$  of 1/s and 10/s are nearly superposed. Softening and complete stress relaxation occur under tensile and shear loading due to damage accumulation. Slight oscillations occur in the tension and compression stress–strain curves due to lateral stress relief waves from the Poisson effect and the dynamic integration scheme.

Maximum crack density  $\omega_C$  and threshold damage parameter  $D_T$  were chosen based on observations from ballistic experiments on the material of interest [58]. In experiments, the typical fragment size was observed to be on the order of the minimum dimension of the coarse aggregate of the concrete microstructure, here 9.5 mm. For cubic fragments, this implies an edge length  $\bar{b}$  of  $9.5/\sqrt{3}$  mm, as the aggregate stones were sized in practice via passage through a sieve with holes of diameter 9.5 mm. A typical strain rate observed over the duration of the fragmentation event was  $\dot{\epsilon} = 2(10)^4/s$ , based on examination of results from simulations reported later in Section 5.1. Invoking (32), and assuming that fragmentation begins when the material has lost half of its strength, i.e.,  $D_T = 0.5$ , then produces the value of  $\omega_C$  listed in Table 1. More quantitative experiments on damage evolution and fragmentation are needed to support independent choices of  $\omega_C$  and  $D_T$ ; however, for the present scenarios of

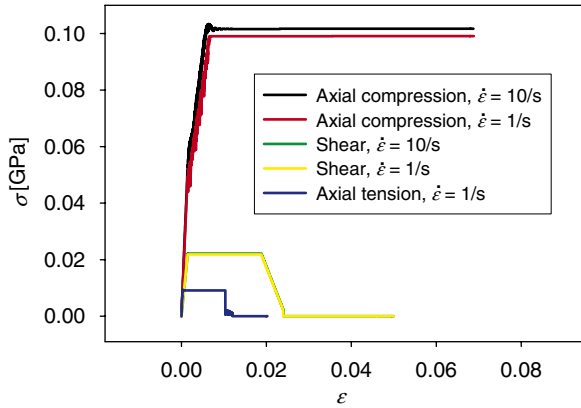


Fig. 6. Computed dynamic stress–strain ( $\sigma - \epsilon$ ) response.

interest, the choice of parameters insignificantly affects the model predictions apart from the mean fragment dimension. Others have suggested a correlation between grain or aggregate size and typical or minimum fragment dimension in granular geological materials [69].

#### 4.2. Numerical implementation

The material model was inserted into the 2003 version of the EPIC Lagrangian finite element code [47,62]. The equations of motion and constitutive response are integrated explicitly, and GPA and contact algorithms are available for addressing multi-body interactions.

The stress rate is derived by differentiating (17) and assuming small elastic stretch, giving

$$\dot{\hat{\boldsymbol{\sigma}}} = 2G(1 - D)\hat{\mathbf{D}}^E + \mathbf{W}^E\hat{\boldsymbol{\sigma}} - \hat{\boldsymbol{\sigma}}\mathbf{W}^E - \dot{D}\hat{\boldsymbol{\sigma}}/(1 - D), \quad (58)$$

where  $\hat{\mathbf{D}}^E$  is the symmetric, deviatoric part of  $\mathbf{L}^E$  and  $\mathbf{W}^E$  is the skew part of  $\mathbf{L}^E$ . The assumption of small elastic strains is standard in metal plasticity literature [33], has been widely used for concrete modeling [12], and enables efficient integration of the deviatoric stress state via a radial return algorithm. The assumption is thought to be justified here for concrete deforming in shear or tension in that yielding and failure of the material should occur prior to the attainment of large deviatoric stresses (and correspondingly large deviatoric elastic strains), from evolving inelastic deformation (20) and damage  $D$  in (21).

Under realistic cases where elastic volume changes are large, e.g., triaxial compression, the hydrostatic pressure is of primary interest. At large pressures, the hydrostatic response is integrated in terms of the modified total volumetric strain  $\bar{\mu}$ , following [7]:

$$\bar{\mu} = (\mu - \varphi_L)/(1 + \varphi_L). \quad (59)$$

At pressures beneath the locking pressure, elastic strains are small, and a relationship equivalent to (18) is used. On the other hand, a direct cubic fit to the Hugoniot data of [64] is invoked, via  $p = K_1\bar{\mu} + \hat{K}_2\bar{\mu}^2 + K_3\bar{\mu}^3$ , at high pressures and large elastic compressive strains, after all porosity is compacted. In this way, possible errors due to

linearization of elastic strain propagated from (58) are avoided in the high pressure–volume response. Note from Table 1 that  $\hat{K}_2$  differs from  $K_2$  by 20 GPa due to the choices of volumetric strain measures used at low (5) and high (59) pressures.

The energy balance (13) is exercised, along with thermodynamic expressions (23) and (26), to update the temperature of the material. To this end, the elastic strain quantities of (5), and hence the elastic deformation gradient  $\mathbf{F}^E$ , are needed. The latter is computed via an exponential update standard in the context of computational crystal plasticity [24,70]. The following approximations are used here:

$$\mathbf{F}_{t+\Delta t}^E = \exp(\mathbf{L}^E \Delta t) \mathbf{F}_t^E, \\ \exp(\mathbf{L}^E \Delta t) = \mathbf{1} + \frac{\sin \Omega}{\Omega} \mathbf{L}^E \Delta t + \frac{1 - \cos \Omega}{\Omega^2} (\Delta t)^2 (\mathbf{L}^E)^2, \quad (60)$$

where  $\Delta t$  is the time increment of integration,  $\mathbf{L}^E$  is assumed constant over the time increment, and  $\Omega = \sqrt{(1/2)\mathbf{L}^E : \mathbf{L}^E} \Delta t$ . In the present application of (60),  $\mathbf{L}^E$  is computed by subtracting the plastic deformation rate from the total velocity gradient, thereby including all rigid body rotations in the elastic part of the deformation. One can show that the form of (60)<sub>2</sub> is exact when  $\mathbf{L}^E$  is skew, and otherwise introduces numerical error of order  $(\Delta t)^3$  that is negligible in the context of dynamic calculations of the sort here, for which  $\Delta t$  is very small. Also, since the elastic stretch generally remains small in the large scale computations that follow in Section 5, in these computations  $\mathbf{L}^E$  consists predominantly of rotation and is nearly skew.

The following methodology for addressing failure of the material is used. When an integration point achieves a critical value of damage, i.e. when  $D = 1$ , failure occurs. Failed material supports no deviator stresses or tensile pressures. In practice, when  $D > 0.95$  in the numerical integration,  $D$  is subsequently set to unity and the material fails in the next integration cycle, in order to avoid difficulties with (58) as  $D$  approaches unity. Additionally, finite elements are converted into particle nodes when a scalar measure of effective inelastic or volumetric strain, termed the erosion strain, is attained [47,62], in order to alleviate numerical inaccuracies associated with highly distorted elements. In the calculations that follow, the erosion strain is chosen as 0.5, following recommendations in [62]. For the present material model, failure may or may not necessarily precede erosion, but eroded elements are almost always failed, as  $D$  in (20) typically attains a value of unity prior to accumulation of sufficient strain needed to trigger particle conversion.

Two methods have been developed for addressing fragment mass and velocity distributions. For the approach of Section 3.1, a typical fragment dimension is computed for each converted particle using Eq. (32), where the strain rate  $\dot{\epsilon}$  during the fragmentation event is time-averaged only over explicit integration cycles for which

$D > D_T$ . The number of fragments associated with a given particle is then found by dividing the particle's mass by the mass of its associated fragment. Each fragment is assigned the velocity of its parent particle. For the statistical approach of Section 3.2, the total mass and mass-weighted velocity of the particle cloud (see later Eq. (62)) are extracted from the simulation output. The total number of fragments follows from assumption of a nominal fragment dimension corresponding to the aggregate size as discussed above. Then upon application of (57), all quantities in distribution (52) are known, and the velocity and mass probability distributions are computed in a post-processing step.

The presentation here has emphasized the general theory, with more restrictive assumptions that narrow the focus of the model to a particular concrete material introduced only as they become necessary. This enables avenues for extending the framework to related materials in the future, and also permits description of the limitations of the specific material model and its numerical implementation. Note that while the nonlinear elastic theory was implemented numerically for hydrostatic deformations in order to select bulk elastic constants (Figs. 2 and 3) and judge the thermodynamic admissibility of porosity evolution (Fig. 5), some simplifications have been enacted to enable solution of large scale problems encompassing

hundreds of thousands of elements and particles. Specifically, these include Eqs. (58), (59), and the failure algorithm discussed above. Table 2 lists the general scheme and corresponding equations used for the constitutive update in the large scale calculations presented in Section 5. These steps in the computation are bypassed, for the most part, once local failure of the material has occurred. In Table 2,  $t = t_F$  denotes the time instant in the solution at which fragmentation commences, when the damage  $D$  attains or surpasses a threshold value of  $D_T$ . It is also noted that all numerical implementations rely on some approximation of the governing differential equations, e.g., discretization in space and time, and the present computations, in the context of coupled finite elements and meshless particles, are of course subject to such universal limitations.

## 5. Numerical simulations

Two problems were used to demonstrate the capabilities of the concrete material model. The first involved perforation of a concrete target by a spherical metallic projectile; the second involved fragmentation of a spherical concrete projectile upon impact with a metallic plate.

### 5.1. Concrete perforation

A specific initial-boundary value problem was solved to mimic a ballistic perforation experiment conducted at the US Army Research Laboratory (ARL) [58]. In the experiment, a small tungsten sphere was fired at concrete wall. The sphere, of diameter 7.94 mm, was formed from an alloy of mass density 18 690 kg/m<sup>3</sup>. The concrete target was SAC-7 composition [6], with no reinforcing bars, 25.4 mm thick. High-speed photography was used to record the striking velocity of the projectile, measure the residual velocity of the penetrator, and collect images of the fragment debris cloud. Post-mortem measurements of hole and crater dimensions were obtained via visual inspection.

The initial problem geometry is shown in Fig. 7. The concrete target's dimensions were 25.4 mm × 102 mm × 102 mm, with half modeled explicitly as a result of symmetry. Two meshes were used to evaluate effects of mesh density: a coarse grid with 102 144 composite tetrahedral elements [62] and a fine grid with 244 512 elements. The mesh density in the target was reduced gradually with increasing distance from the location of impact. The impact velocity of the sphere was 1120 m/s. Frictionless contact between projectile and target was assumed. Adiabatic conditions were invoked, with a uniform initial temperature of 294 K.

The constitutive model used for the concrete, as developed in Sections 2–4, is the focus of this work and was used to model the target. On the other hand, a simple yet efficient and widely used constitutive model was chosen for modeling the behavior of the projectile. Specifically, the alloy of the sphere was modeled using the constitutive theory of Johnson and Cook [9] for the deviatoric

Table 2  
Steps used in constitutive update for large scale computations

Step	Equation(s)
Read in constants, internal variables, and rate variables	–
Compute effective shear modulus	$G \rightarrow G(1 - D)$
Compute effective flow stress	(20)
Compute deviatoric Cauchy stress	$\hat{\boldsymbol{\sigma}} = \boldsymbol{\sigma} - (\text{tr } \boldsymbol{\sigma}/3)\mathbf{1}$
Update stress using radial return algorithm	(58)
Update inelastic deformation rates	(2), with $2\mathbf{L}^D = \mathbf{F}^D \mathbf{F}^{D-1} + \mathbf{F}^{D-T} \mathbf{F}^{D^T}$
Update plastic work	(25)
If $\varphi = \varphi_L$ , compute effective bulk modulus and pressure	(15), (18)
If $\varphi = \varphi_L$ , compute effective volume change and pressure	(59), with $p = K_1 \bar{\mu} + \hat{K}_2 \bar{\mu}^2 + K_3 \bar{\mu}^3$
Update elastic deformation gradient	(60)
Compute elastic volume change and elastic strain deviator	(5), $\hat{\mathbf{E}}^E = \mathbf{E}^E - (\vartheta_E/3)\mathbf{1}$
Update porosity and damage	(21)
Add dissipation from rates of porosity and damage	(23), (26)
Update internal energy	(13)
If $D > D_T$ , update cumulative strain during fragmentation	$\varepsilon_{t+\Delta t} = \varepsilon_t + \Delta t \sqrt{\mathbf{D} : \mathbf{D}}$
If $D > D_T$ , update rate over fragmentation time span, $t - t_F$	$\dot{\varepsilon} = \varepsilon_{t+\Delta t} / (t + \Delta t - t_F)$
If $D > D_T$ , compute fragment size and number of fragments	(32), $N = M / (\rho \bar{b}^3)$
If $D = 1$ , zero deviator stresses and tensile pressure	$\hat{\boldsymbol{\sigma}} \rightarrow \mathbf{0}$ , $p \in (p < 0) \rightarrow 0$

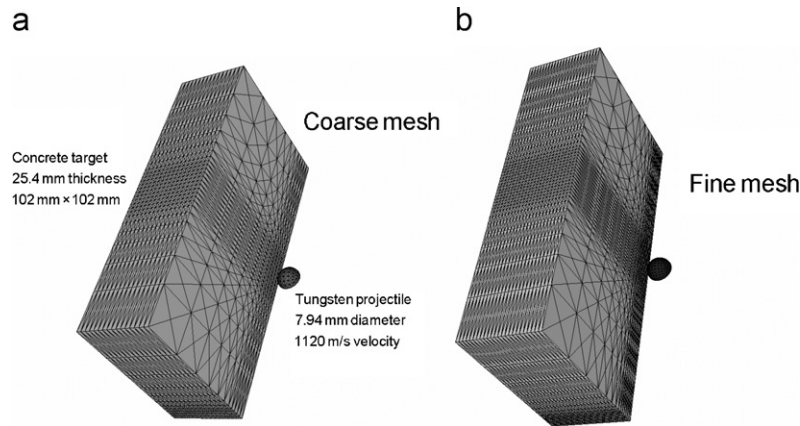


Fig. 7. Ballistic initial-boundary value problem: (a) coarse mesh, 102 144 elements, and (b) fine mesh, 244 512 elements.

Table 3  
Experimental and numerical results, ballistic impact and fragmentation

	Experiment	Simulation, coarse	Simulation, fine
Penetrator $V_R$ (m/s)	854	814	825
Hole diameter (mm)	21	25	26
Crater diameter (mm)	55	52	50
Mass loss $M_L$ (kg)	0.1	0.134	0.123
Eroded mass $M$ (kg)	—	0.014	0.014
Avg. frag. velocity $\bar{v}$ (m/s)	—	133	116

mechanical response, with a Mie–Gruneisen equation of state for the hydrostatic response [62]. As the tungsten sphere did not fracture or degrade significantly during the experiment, failure of the tungsten was suppressed in the simulations. Properties were those for a tungsten alloy from the EPIC library [9,62], apart from the mass density, which was set to exactly match that of the experimental specimen. It is noted that the constitutive updates of the material responses tended to require little execution time relative to particle search algorithms as the solutions proceeded and numerous finite elements were converted to meshless particles.

Results from experiment and simulations are compared in Table 3. The magnitude of the residual velocity of the spherical projectile,  $V_R$ , agreed within 5% between simulations and experiment, with a difference of less than 1.5% between simulations with fine and coarse grids. Hole and crater diameters corresponded to the exit side of the target. The hole diameter was estimated experimentally and in the simulations as the visible diameter of perforation. The crater diameter was measured experimentally as is clear from visual inspection of Fig. 8(a). The simulated crater diameter was estimated as that part of the target surrounding the perforation where the material was fully or nearly fully damaged, i.e., where  $D \approx 1$ . This region is shown by darkened grayscale values in Fig. 8(b). Converted particles are deliberately not shown in Fig. 8(b). It is

suggested here that such fully damaged material, as it supports no tensile or deviatoric stresses, would simply fall off the target after the impact event due to the force of gravity, leaving behind a crater in the concrete. The total mass lost in the experiment was determined by weighing the target before and after the test and subtracting the post-test weight from the initial weight. The mass loss in the simulation was computed via

$$M_L = \int \rho D dV, \tag{61}$$

where the domain of integration is the volume of target material, and damaged material was considered to contribute to mass loss following the above arguments. The eroded mass  $M$  reported in the simulations was simply the summed mass of all particle nodes, while the average velocity magnitude of the fragment cloud was computed by

$$\bar{v} = M^{-1} \sum_k m_k v_k, \tag{62}$$

where the velocity  $v_k$  of each particle  $k$  was weighed by that particle’s mass  $m_k$ . Numerical results in Table 3 correspond to the solution time  $t = 150 \mu s$ , as values of these quantities (e.g., average projectile and fragment velocities and dimensions derived from damage contours) did not change significantly at increments beyond this instant of time in the calculations.

Photographs from the ballistic experiment are shown in Fig. 9. The projectile is exiting the target and traveling from left to right in this series of frames. Initially, some fragment debris is propelled ahead of the projectile (Fig. 9(a)), but as the fragmentation event proceeds, the projectile passes through much of the debris cloud (Figs. 9(b) and (c)). The fragment cloud appears close to co-linear with the path of the projectile, in agreement with prior assumptions in the statistical model, though there is some spread (i.e., non-zero cone angle). The fastest moving particles appear small, powder-like, and are thought to consist mainly of pulverized mortar. Larger, slower-moving particles remain closer to the target in the

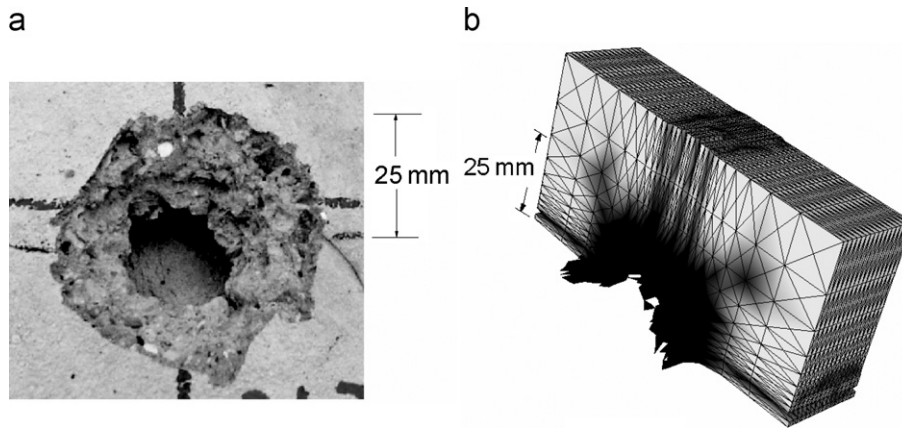


Fig. 8. Post-event crater: (a) experiment [58] and (b) simulation. Darkened areas in grid (b) denote damage state variable  $D$ .



Fig. 9. Fragmentation event: high-speed photos from ballistic experiment [58].

Fig. 9(c), and are thought to consist mainly of aggregate chunks. Photographs of the ballistic event were not available on the entrance side of the target, though substantial debris was observed there post-test.

Results from a simulation are visualized in Fig. 10, at  $t = 150 \mu\text{s}$ , corresponding to the experimental image in Fig. 9(c). The simulation with the coarse mesh is depicted; corresponding results for the fine mesh were visually very similar. Concrete particles are scaled in the figure by the nominal fragment diameter  $\bar{b}$ , as computed from the energetic theory, Eq. (32). Particles are colored by velocity magnitude. As observed in the experiment, the penetrator's exit velocity exceeds that of most of the concrete fragments. Larger fragments are slower-moving and remain close to the target, while fast moving fragments are relatively smaller in size. Note that the effects of aerodynamic resistance, which presumably could impart drag on small particles with large surface area to volume ratios, are not included in the simulations. Such effects would presumably reduce the speed of very fast moving particles that exceed the projectile's velocity in the simulation. Contours of damage  $D$  are shown in the concrete target. A few particles that appear stray in Fig. 10 were in fact ejected from the sides of the target where damage propagated to the edges. The most fully damaged material logically surrounds the perforation, though the damage pattern is not purely axisymmetric due to the non-symmetric construction of the mesh and the rectangular geometry of the target.

Mass probability distributions for the fragment cloud are shown in Fig. 11(a). The distributions were computed in two different ways: the energetic theory of Section 3.1 and the statistical physics-based theory of Section 3.2. For the energetic theory, the mass of all fragments comprising a particle  $k$  was computed from (32) as

$$m_k = \left[ \frac{K_C^2 \omega_C (D - D_T)}{8 K_E \rho^{1/3} \dot{\epsilon}^2} \right]_k^{3/2}. \tag{63}$$

Subsequently, distributions were generated by grouping fragments into bins organized by mass:

$$\bar{p}(m_1 < m < m_2) = M^{-1} \sum_j m_j, \tag{64}$$

where  $j$  spans all fragments with masses in the range  $m_1 < m < m_2$ . For the statistical theory, corresponding probability distributions were found from (52) as

$$\begin{aligned} \bar{p}(m_1 < m < m_2) &= \frac{1}{M} \int_{m_1}^{m_2} \int_0^\infty m \hat{p}(m, v) dv dm \\ &= - \left( \frac{m}{M} + \frac{1}{N} \right) \exp \left( \frac{-N}{M} m \right) \Big|_{m_1}^{m_2}, \end{aligned} \tag{65}$$

where the total mass  $M$  is listed in Table 3. The results of Fig. 11(a) may be interpreted as follows. As predicted by the energetic theory using numerical results from the coarse grid, for example, fragments having masses between 0.0001 and 0.001 kg constitute 48% of the total mass of the

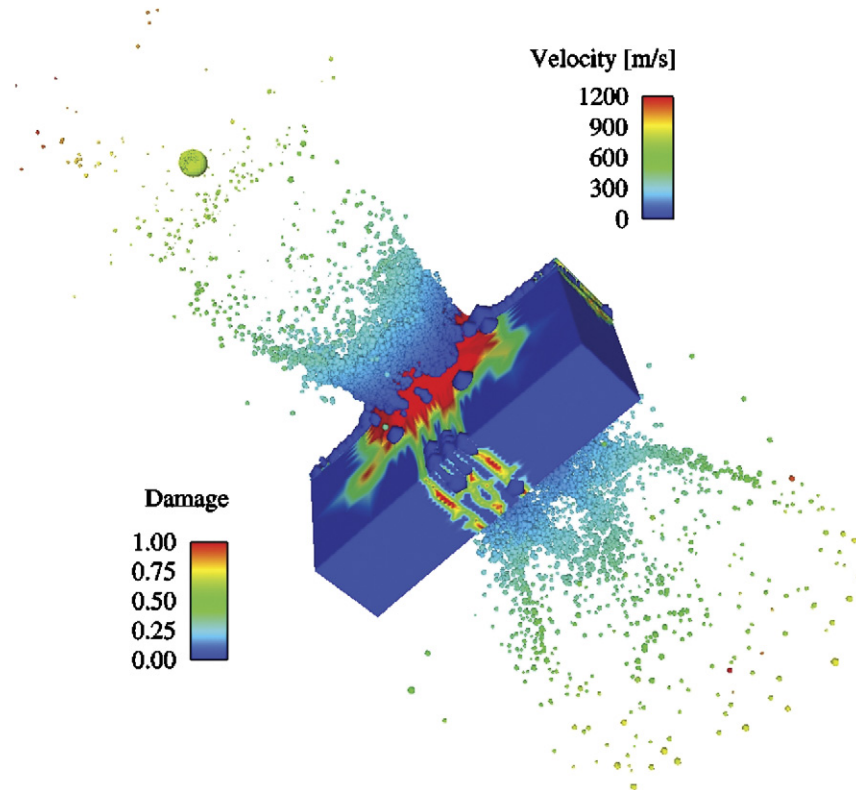


Fig. 10. Fragmentation event: simulation at 150 μs. Particle diameter scaled by fragment dimension and particles colored by velocity magnitude. Penetrator elements colored by velocity magnitude. Concrete target elements colored by damage variable  $D$ .

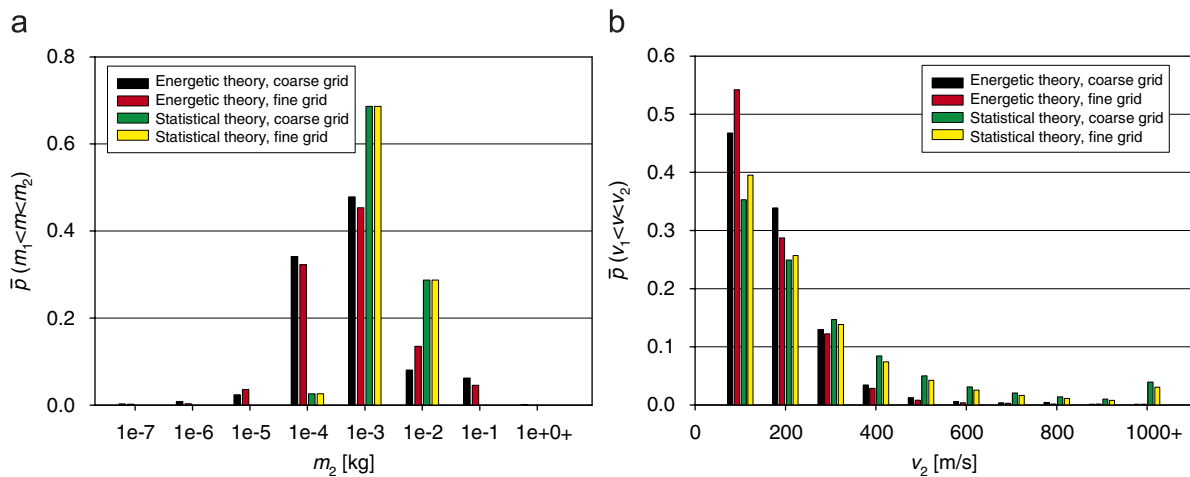


Fig. 11. Predicted fragment: (a) mass and (b) velocity distributions at 150 μs.

fragment cloud. Slight differences in mass probabilities among simulations with coarse and fine grids are evident in the energetic theory, on the order of a few percent at most for any particular bin. However, since an identical value of  $M$  was computed in both simulations, the statistical theory yielded identical results for coarse and fine discretizations. Note that for all four cases (i.e., two theories and two grid sizes), the bin containing the largest mass fraction of fragments was that for which fragments spanned the range of  $0.0001 \text{ kg} < m < 0.001 \text{ kg}$ .

Velocity probability distributions of the fragment debris are shown in Fig. 11(b). These are mass-weighted distributions. For the energetic theory, the probability was computed by

$$\bar{p}(v_1 < v < v_2) = M^{-1} \sum_k m_k, \tag{66}$$

where the index  $k$  here identifies a particle whose velocity is within the range  $v_1 < v < v_2$ , with mass of that particle denoted by  $m_k$ . For the statistical physics theory, individual

particle velocities were not considered directly. Instead the global center of mass velocity  $\bar{v}$  of Eq. (62) and Table 3 was substituted into (57) to compute the kinetic energy distributed among the fragments. The probability was then estimated from Eq. (52) as

$$\bar{p}(v_1 < v < v_2) = N^{-1} \int_{v_1}^{v_2} \int_0^\infty \hat{p}(m, v) dm dv = \sqrt{(3N)/(4E)} \times [v / \sqrt{(N/M) + (3Nv^2)/(4E)}]_{v_1}^{v_2}. \quad (67)$$

Fig. 11(b) shows the predicted mass fraction of fragments within a particular velocity range. For example, from the energetic theory with a coarse mesh, 47% of the mass of the cloud should exhibit a velocity magnitude in the range 0–100 m/s, and 34% in the range of 100–200 m/s. Slight differences between velocity  $\bar{v}$  for simulations with coarse and fine meshes led to differences in their statistical physics-based predictions, for example on the order of a 4% for the computed value of  $\bar{p}$  for the mass fraction of fragments with  $v < 100$  m/s. Predictions from the energetic theory differed slightly more with mesh density, on order of 8%, for example, for the mass fraction of fragments with  $v < 100$  m/s. Note that for all four cases, the bin of range  $0 < v < 100$  m/s was predicted to contain the largest mass fraction of fragments.

## 5.2. Dynamic impact crushing

Because quantitative data on fragment mass distributions were not available from the experiment [58] simulated above, a second simulation was performed to further judge the accuracy and limitations of aspects of the present model. The experiment was conducted elsewhere, as described in [3], in an investigation of methods for reducing concrete rubble to recyclable form via impact crushing. In the experiment [3], a concrete sphere was propelled at moderate velocity into a target plate within a cylindrical catch tank; upon impact of the sphere with the plate, the concrete fractured and fragmented into debris that were collected from the tank. Multiple passes through the apparatus were used to further reduce the rubble. Here, only the first pass is simulated, and the interactions between concrete projectile and metallic tank are limited to the initial impact of the sphere with a flat plate. Subsequent interactions that would presumably occur in the experiment, such as impact of the fragments with the sides of the tank upon ricochet, are not modeled here.

The same modeling procedures developed in Sections 2–4 were used here. Elastic, plastic, and damage evolution relationships and properties for SAC-7 concrete [6] were employed in the simulation, as experimental data on the strength of the concrete tested in [3] were not reported. For this reason, discrepancies may naturally emerge between results of simulation and experiment. Specifically, it is noted that the compositions appear different in [3] and [6], with different types of aggregate and mortar. In order to predict the fragment mass distributions, only the method

predicated upon a local energy balance (Section 3.1) was used here. Since the fragment clouds are far from 1D (52) or spherical [57], analytical statistical physics-based theories of the sort derived in Section 3.2 do not immediately apply.

The problem consisted of a spherical concrete projectile of diameter 150 mm impacted against a steel wall of dimensions 100 mm × 750 mm × 750 mm at a normal velocity of 55 m/s. Two meshes of increasingly fine discretization were used. The coarse mesh consisted of 34 272 elements, while the fine mesh included 81 408 elements. As in the previous problem of Section 5.1, all elements were composite tetrahedral [53], and mesh densities in the target were reduced gradually with increasing distance from the location of impact. Frictionless contact between projectile and target was assumed, and adiabatic conditions were invoked, with a uniform initial temperature of 294 K. The target plate was assumed to consist of 4340 steel, addressed here with standard Johnson–Cook plasticity [9] and fracture [10] models and properties from the EPIC material library. The coarse mesh is shown in Fig. 12(a).

The deformed coarse mesh, with converted particles, is shown in Fig. 12(b), at  $t = 5$  ms after impact. Fragment mass distributions remained nearly static at later solution times. Particle diameters are scaled by their corresponding fragment size  $\bar{b}$  in Fig. 12(b). Note that each visually smaller particle in fact often represents a cloud of many small particles, since the nodal mass of each particle is distributed among the multiple fragments corresponding to that particle. From Fig. 12(b) a mixed distribution of fragment sizes is apparent. The concrete debris consists of small faster-moving fragments on the periphery, large generally slower-moving fragments near the center of the target plate, and several intact pieces of the projectile. The latter are finite elements that did not fail or convert to particles in the simulation.

Predicted fragment mass distributions, computed from Eq. (64), are compared with those obtained from the experiment [3] in Fig. 13. Bins used to group the fragments here are the same used in [3], where fragment diameters from [3] have been converted to masses in Fig. 13 via the mass density of SAC-7 concrete listed in Table 1,  $\rho_0 = 2440$  kg/m<sup>3</sup>. From Fig. 13, the model appears to predict the fragment mass distributions with reasonable accuracy. The relatively large concentration  $\bar{p} \approx 0.4$  of larger fragments in the range of  $0.02$  kg  $< m < 1.3$  kg results mainly from the unconverted finite elements of the concrete sphere (perhaps damaged but not failed). These pieces were included in the fragment count, since in the experiment the entire specimen was apparently sieved during fragment collection from the catch tank. The relatively large concentration  $\bar{p} \approx 0.35$  in the intermediate range of  $0.00004$  kg  $< m < 0.0025$  kg emerges from the balance of fracture energy and kinetic energy fueling the local fragmentation process in (32); i.e., most of the converted particles fall into this bin. The fraction of smaller

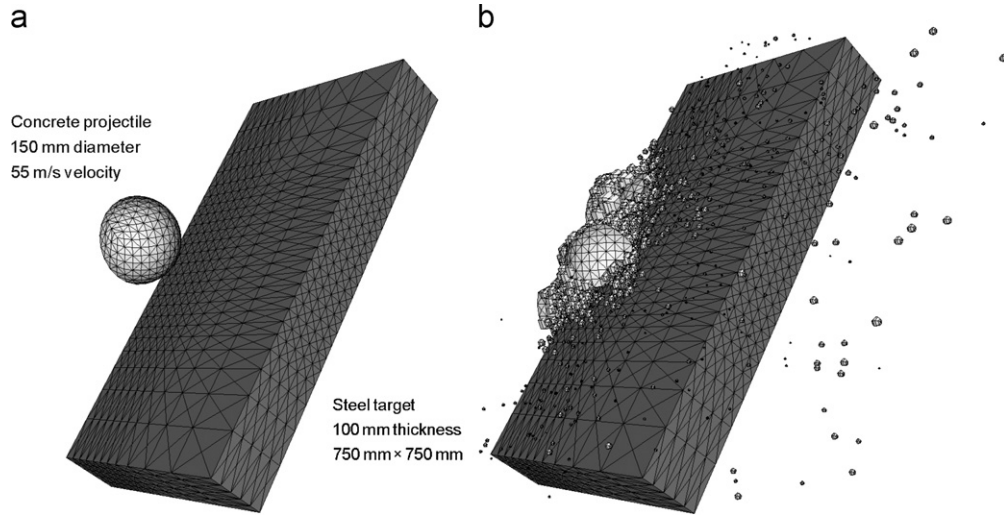


Fig. 12. Impact crushing of concrete sphere: (a) initial conditions and (b) fragmentation event at 5 ms, with particle diameters scaled by fragment dimension.

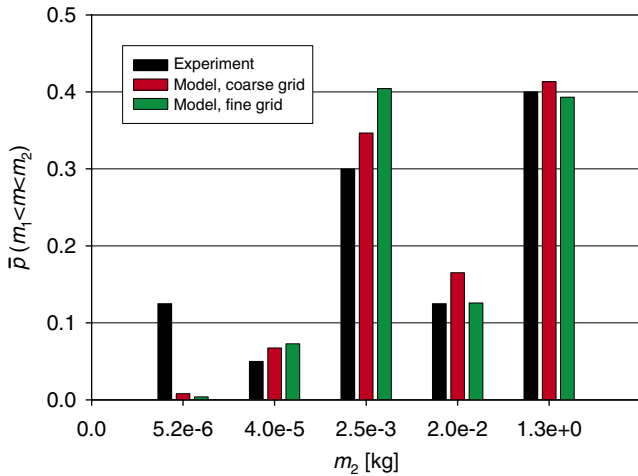


Fig. 13. Fragment mass distributions from impact crushing of concrete sphere (experimental data from [3]).

fragments,  $m < 5.2(10)^{-6}$  kg, is vastly under-predicted by the theory. This is because local strain rates achieved during integration cycles over which  $D > D_T$  were of insufficient magnitude to generate very small fragments via (32). This effect highlights the limitation of the present modeling approach: only dynamic high-rate fragmentation problems can be simulated, as the local kinetic energy of the material, balanced by the energy dissipated by micro-cracking, provides the sole impetus for break up into numerous fragments. It is noted that very small fragments could feasibly be generated in the experiments by interactions with the walls of the catch tank upon ricochet and settling, effects not modeled here. It is also noted that explicit radial crack patterns reported from high-speed photographs in [3] cannot be reproduced by the present framework based on continuum damage mechanics. Some mesh dependence is evident, but not excessive, in Fig. 13: differences among predictions of  $\bar{p}(m)$  obtained from fine

and coarse meshes of no more than 6% are apparent in any bin.

Fragment velocity data were not available from the experimental description [3]; hence such data, though available from the computation, are not presented here. Experimental velocity data appear scarce for dynamic fragmentation of pure (not reinforced) concrete of interest here. However, some experimental data are available for colliding rocks [57,71] and bar-reinforced concrete walls undergoing explosive loading [2].

## 6. Conclusions

A constitutive theory for deforming and fragmenting crushable solids has been developed. The theory includes the following novel combination of features: finite deformation kinematics of elasticity, plasticity, and inelastic compression; an energy density function with contributions from nonlinear elasticity, damage, and porosity; and kinetic relations for evolution of inelastic deformation, pore compression, and damage satisfying both the energy balance and entropy inequality. The theory also features two alternative, physically motivated methods to compute fragment size and velocity distributions. In the energetic method, a local balance between expansion kinetic energy and fracture energy associated with damage evolution leads to a local fragment size. In the statistical method, global entropy maximization leads to a joint mass–velocity distribution function. The theory has been implemented in a Lagrangian FE setting with GPA, whereby highly distorted elements are converted to interacting particle nodes. In the implementation of the plasticity theory, small elastic strain assumptions are used, though the hydrostatic response, computed separately, is considered valid to large pressures. Local/global solution data from converted GPA nodes are used to compute

fragment size and velocity distributions for the energetic/statistical methods, respectively.

The model was first used to study the impact of a small tungsten sphere into a thin concrete target. Residual projectile velocities, hole and crater dimensions, and target mass loss were comparable between experiment and two simulations of different mesh density. Attributes of the fragment debris clouds agreed qualitatively among simulations and experiment, with the fastest particles usually being smallest in size. Distributions of mass and velocity were computed using the two thermodynamically motivated methods (energetic and statistical), and two grid spacings (coarse and fine). Mass-weighted distributions were qualitatively similar among all cases, with the bin corresponding to the largest fraction of fragments having a particular mass or velocity range the same regardless of method or mesh size. Predictions of mass distribution were fairly mesh-independent, with velocity slightly more so (e.g., maximum velocity probability differences on the order of 8% for a 140% increase in number of elements). It remains to be seen which fragmentation theory most closely replicates live ballistic perforation experiments as experimental mass and velocity distribution data become more available.

In a second simulation, the energetic method was used to predict fragment mass distributions upon impact crushing of a concrete sphere. Following quantitative comparison with experimental data, the theory predicted mass distributions of larger fragments with reasonable success, despite uncertainty in the strength properties of the concrete tested in the experiment. However, the model failed to capture very small fragment debris produced in the experiment, as sufficiently high deformation rates needed to yield very small fragments were not attained in the simulation. This artifact of the model illustrates that modifications to the present framework are needed to properly address failure and fragmentation under quasi-static and low-strain-rate loading conditions.

## Acknowledgments

This work was supported by the US Army Research Laboratory (ARL). R. Moxley and R. Phillabaum are acknowledged for providing data and photographic images from the concrete penetration experiment that was conducted jointly by researchers employed by ARL and the US Army Engineer Research and Development Center (ERDC).

## References

- [1] Davidson JS, Porter JR, Dinan RJ, Hammons MI, Connell JD. Explosive testing of polymer retrofit masonry walls. *J Perform Constructed Facilities* 2004;18:100–6.
- [2] Xu K, Lu Y. Debris velocity of concrete structures subjected to explosive loading. *Int J Numer Anal Meth Geomech* 2006;30:917–26.
- [3] Tomas J, Schreier M, Gröger T, Ehlers S. Impact crushing of concrete for liberation and recycling. *Powder Technol* 1999;105:39–51.
- [4] Momber AW. The fragmentation of standard concrete cylinders under compression: the role of secondary fracture debris. *Eng Fract Mech* 2000;67:445–59.
- [5] Carpinteri A, Lacidogna G, Pugno N. Scaling of energy dissipation in crushing and fragmentation: a fractal and statistical analysis based on particle size distribution. *Int J Fract* 2004;129:131–9.
- [6] Hanchak SJ, Forrestal MJ, Young ER, Ehgott JQ. Perforation of concrete slabs with 48 MPa (7 ksi) and 140 MPa (20 ksi) unconfined compressive strengths. *Int J Impact Eng* 1992;12:1–7.
- [7] Holmquist TJ, Johnson GR, Cook WH. A computational constitutive model for concrete subjected to large strains, high strain rates, and high pressures. In: Murphy MJ, Backofen JE, editors. Proceedings of the 14th international symposium on ballistics. Quebec City, Canada, USA: American Defense Preparedness Association (ADPA), 1993. p. 591–600.
- [8] Williams EM, Akers SA, Reed PA. Laboratory characterization of fine aggregate cementitious material. ERDC/GSL Technical Report-05-16; 2005, approved for public release.
- [9] Johnson GR, Cook WH. A constitutive model and data for metals subjected to large strains, high strain rates, and high temperatures. In: Proceedings of the 7th international symposium on ballistics, The Hague, Netherlands, USA: American Defense Preparedness Association (ADPA), 1983. p. 541–7.
- [10] Johnson GR, Cook WH. Fracture characteristics of three metals subjected to various strains, strain rates, temperatures, and pressures. *Eng Fract Mech* 1985;21:31–48.
- [11] Grote DL, Park SW, Zhou M. Dynamic behavior of concrete at high strain rates and pressures: I. experimental characterization. *Int J Impact Eng* 2001;25:869–86.
- [12] Park SW, Xia Q, Zhou M. Dynamic behavior of concrete at high strain rates and pressures: II. numerical simulation. *Int J Impact Eng* 2001;25:887–910.
- [13] Bažant ZP, Caner FC, Carol I, Adley MD, Akers SA. Microplane model M4 for concrete. I. formulation with work-conjugate deviatoric stress. *ASCE J Eng Mech* 2000;126:944–53.
- [14] Asaro RJ. Crystal plasticity. *ASME J Appl Mech* 1983;50:921–34.
- [15] Bažant ZP, Caner FC, Adley MD, Akers SA. Fracturing rate effect and creep in microplane model for dynamics. *ASCE J Eng Mech* 2000;126:962–70.
- [16] Bažant ZP, Adley MD, Caner FC, Carol I, Jirásek M, Akers SA, et al. Large-strain generalization of microplane model for concrete and application. *ASCE J Eng Mech* 2000;126:971–80.
- [17] Voyiadjis GZ, Abu-Lebdeh TM. Damage model for concrete using bounding surface concept. *ASCE J Eng Mech* 1993;119:1865–85.
- [18] Feenstra PH, De Borst R. Composite plasticity model for concrete. *Int J Solids Structures* 1996;33:707–30.
- [19] Momber AW. The efficiency of mechanical concrete comminution. *Eng Fract Mech* 2003;70:81–91.
- [20] Lee EH, Liu DT. Elastic-plastic theory with application to plane-wave analysis. *J Appl Phys* 1967;38:19–27.
- [21] Coleman BD, Noll W. The thermodynamics of elastic materials with heat conduction and viscosity. *Arch Ration Mech Anal* 1963;13:167–78.
- [22] Coleman BD, Gurtin M. Thermodynamics with internal state variables. *J Chem Phys* 1967;17:597–613.
- [23] Scheidler M, Wright TW. A continuum framework for finite viscoplasticity. *Int J Plasticity* 2001;17:1033–85.
- [24] Clayton JD. Dynamic plasticity and fracture in high density polycrystals: constitutive modeling and numerical simulation. *J Mech Phys Solids* 2005;53:261–301.
- [25] Passmann PL, Grady DE, Rundle JB. The role of inertia in the fracture of rock. *J Appl Phys* 1980;51:4070–5.
- [26] Kachanov LM. On the time to failure under creep conditions. *Izv Akad Nauk SSSR Otd Tekh Nauk Metall Topl* 1958;8:26–31.

- [27] Lemaitre J, Chaboche J-L. *Mecanique des Materiaux Solides*: Dunod, Paris, 1985.
- [28] Krajcinovic D. *Damage mechanics*. Amsterdam, The Netherlands: North-Holland; 1996.
- [29] Rajendran AM, Grove DJ. Modeling the shock response of silicon carbide, boron carbide, and titanium diboride. *Int J Impact Eng* 1996;18:611–31.
- [30] Krajcinovic D, Rinaldi A. Statistical damage mechanics—part I: theory. *ASME J Appl Mech* 2005;72:76–85.
- [31] Brannon RM. A consistent kinetics porosity (CKP) model. Sandia Report 1999-1493C, Albuquerque, NM; 1999.
- [32] Brannon RM. The consistent kinetics porosity (CKP) model: a theory for the mechanical behavior of moderately porous solids. Sandia Report 2000-2696, Albuquerque, NM; 2000.
- [33] Bammann DJ, Chiesa ML, Horstemeyer MF, Weingarten LI. Failure in ductile materials using finite element methods. In: Jones N, Wierzbicki T, editors. *Structural crashworthiness and failure*. London: Elsevier Applied Science; 1993. p. 1–53.
- [34] Moran B, Ortiz M, Shih CF. Formulation of implicit finite element methods for multiplicative finite deformation plasticity. *Int J Numer Meth Eng* 1990;29:483–514.
- [35] Johnson GR, Cook WH. Recent EPIC code developments for high velocity impact: 3D element arrangements and 2D fragment distributions. *Int J Impact Eng* 1990;10:281–94.
- [36] Rouabhi A, Tijani M, Moser P, Goetz D. Continuum modeling of dynamic behaviour and fragmentation of quasi-brittle materials: application to rock fragmentation by blasting. *Int J Numer Anal Meth Geomech* 2005;29:729–49.
- [37] Mota A, Klug WS, Ortiz M, Pandolfi A. Finite-element simulation of firearm injury to the human cranium. *Comput Mech* 2003;31:115–21.
- [38] Zhou FZ, Molinari J-F, Ramesh KT. A cohesive model based fragmentation analysis: effects of strain rate and initial defects distribution. *Int J Solids Struct* 2005;42:5181–207.
- [39] Espinosa HD, Zavattieri PD. A grain level model for the study of failure initiation and evolution in polycrystalline brittle materials. Part II: numerical examples. *Mech Mater* 2003;35:365–94.
- [40] Brara A, Camborde F, Klepaczko JR, Mariotti C. Experimental and numerical study of concrete at high strain rates in tension. *Mech Mater* 2001;33:33–45.
- [41] Farhenthold EP, Yew CH. Hydrocode simulation of hypervelocity impact fragmentation. *Int J Impact Eng* 1995;17:303–10.
- [42] Schraml SJ, Meyer HW, Kleponis DS, Kimsey KD. Simulating the formation and evolution of behind armor debris fields. In: Post DE, editors. *Proceedings of the 2005 DoD high performance computing users group conference*, Nashville, TN, USA:DoD HPCMP, 2005, approved for public release.
- [43] Silling SA, Askari E. A meshfree method based on the peridynamic model of solid mechanics. *Comput Struct* 2005;83:1526–35.
- [44] Johnson GR, Stryk RA, Beissel SR. SPH for high velocity impact calculations. *Comput Meth Appl Mech Eng* 1996;139:347–73.
- [45] Rabczuk T, Eibl J, Stempniewsky L. Numerical analysis of high speed concrete fragmentation using a meshfree Lagrangian method. *Eng Fract Mech* 2004;71:547–56.
- [46] Johnson GR, Beissel SR, Stryk RA. A generalized particle algorithm for high velocity impact calculations. *Comput Mech* 2000;25:245–56.
- [47] Johnson GR, Holmquist TJ, Beissel SR. Response of aluminum nitride (including a phase change) to large strains, high strain rates, and high pressures. *J Appl Phys* 2003;94:1639–46.
- [48] Grady DE. Local inertial effects in dynamic fragmentation. *J Appl Phys* 1982;53:322–5.
- [49] Grady DE. The spall strength of condensed matter. *J Mech Phys Solids* 1988;36:353–84.
- [50] Glenn LA, Chudnovsky A. Strain-energy effects on dynamic fragmentation. *J Appl Phys* 1986;59:1379–80.
- [51] Miller O, Freund LB, Needleman A. Modeling and simulation of dynamic fragmentation in brittle materials. *Int J Fract* 1999;96:101–25.
- [52] Mott NF, Linfoot EH. Ministry of Supply, AC 3348; 1943.
- [53] Grady DE, Kipp ME. Geometric statistics and dynamic fragmentation. *J Appl Phys* 1985;58:1210–22.
- [54] Englman R, Rivier N, Jaeger Z. Fragment-size distribution in disintegration by maximum-entropy formalism. *Phil Mag B* 1987;56:751–69.
- [55] Smalley LL, Woosley JK. Application of steady state maximum entropy methods to high kinetic energy impacts on ceramic targets. *Int J Impact Eng* 1999;23:869–82.
- [56] Seaman L, Curran DR, Murri WJ. A continuum model for dynamic tensile microfracture and fragmentation. *ASME J Appl Mech* 1985;52:593–600.
- [57] Grady DE, Winfree NA. Impact fragmentation of high-velocity compact projectiles on thin plates: a physical and statistical characterization of fragment debris. *Int J Impact Eng* 2001;26:249–62.
- [58] Moxley R, Cargile D, Phyllabaum R. Experiment results for the ricochet and perforation of concrete and penetration into damaged concrete by steel fragment projectiles at high velocity. In: *Proceedings of the 77th shock and vibration symposium*, Monterey, CA, Vicksburg, MS, USA:SAVIAC, October 29–November 3, 2006.
- [59] Wu JY, Li J, Faria R. An energy release rate-based plastic-damage model for concrete. *Int J Solids Struct* 2006;43:583–612.
- [60] Gurtin ME, Anand L. A theory of strain-gradient plasticity for isotropic, plastically irrotational materials. Part II: finite deformations. *Int J Plasticity* 2005;21:2297–318.
- [61] Hill R. *The mathematical theory of plasticity*. New York: Oxford University Press; 1950.
- [62] Johnson GR, Stryk RA, Holmquist TJ, Beissel SR. *Numerical algorithms in a Lagrangian hydrocode*. Hopkins, MN: Alliant Techsystems; 1997.
- [63] Sinha BP, Gerstle KH, Tulin LG. Stress-strain relations for concrete under cyclic loading. *J Am Concrete Inst* 1964;61:195–210.
- [64] Marsh SP. *LASL shock Hugoniot data*. CA: University of California Press; 1980.
- [65] Rosakis P, Rosakis AJ, Ravichandran G, Hodowany J. A thermodynamic internal variable model for the partition of plastic work into heat and stored energy in metals. *J Mech Phys Solids* 2000;48:581–607.
- [66] Lu YL, Xu K. Modelling of dynamic behaviour of concrete materials under blast loading. *Int J Solids Struct* 2004;41:131–43.
- [67] Lavenda BH. *Statistical physics, a probabilistic approach*. New York: Wiley; 1991.
- [68] Lambert DE, Ross CA. Strain rate effects on dynamic fracture and strength. *Int J Impact Eng* 2000;24:985–98.
- [69] Astrom JA, Ouchterlony F, Linna RP, Timonen J. Universal dynamic fragmentation in d dimensions. *Phys Rev Lett* 2004;92:245506.
- [70] Becker R. Effects of crystal plasticity on materials loaded at high pressures and strain rates. *Int J Plasticity* 2004;20:1983–2006.
- [71] Waza T, Matsui T. Laboratory simulation of planetesimal collision 2. Ejecta velocity distribution. *J Geophys Res* 1985;90:1995–2011.

NO. OF  
COPIES ORGANIZATION

1 DEFENSE TECHNICAL  
(PDF INFORMATION CTR  
ONLY) DTIC OCA  
8725 JOHN J KINGMAN RD  
STE 0944  
FORT BELVOIR VA 22060-6218

1 US ARMY RSRCH DEV &  
ENGRG CMD  
SYSTEMS OF SYSTEMS  
INTEGRATION  
AMSRD SS T  
6000 6TH ST STE 100  
FORT BELVOIR VA 22060-5608

1 DIRECTOR  
US ARMY RESEARCH LAB  
IMNE ALC IMS  
2800 POWDER MILL RD  
ADELPHI MD 20783-1197

1 DIRECTOR  
US ARMY RESEARCH LAB  
AMSRD ARL CI OK TL  
2800 POWDER MILL RD  
ADELPHI MD 20783-1197

1 DIRECTOR  
US ARMY RESEARCH LAB  
AMSRD ARL CI OK T  
2800 POWDER MILL RD  
ADELPHI MD 20783-1197

ABERDEEN PROVING GROUND

1 DIR USARL  
AMSRD ARL CI OK TP (BLDG 4600)

NO. OF  
COPIES ORGANIZATION

ABERDEEN PROVING GROUND

35 DIR USARL  
AMSRD ARL WM  
J MCCAULEY  
T WRIGHT  
AMSRD ARL WM MD  
B CHEESEMAN  
G GAZONAS  
C YEN  
AMSRD ARL WM TA  
T JONES  
S SCHOENFELD  
AMSRD ARL WM TC  
R COATES  
M FERMEN-COKER  
R PHILLABAUM  
S SCHRAML  
S SEGLETES  
R SUMMERS  
A TANK  
AMSRD ARL WM TD  
S BILYK  
T BJERKE  
D CASEM  
J CLAYTON (10 CPS)  
D DANDEKAR  
M GREENFIELD  
Y HUANG  
B LOVE  
M RAFTENBERG  
E RAPACKI  
M SCHEIDLER  
T WEERASOORIYA

INTENTIONALLY LEFT BLANK.